

Figuring Out Gas & Galaxies in Enzo (FOGGIE). III.
The Mocky Way: Investigating Biases in Observing the Milky Way’s Circumgalactic Medium

YONG ZHENG,^{1,2} MOLLY S. PEEPLES,^{3,4} BRIAN W. O’SHEA,⁵ RAYMOND C. SIMONS,³ CASSANDRA LOCHHAAS,³
LAUREN CORLIES,⁶ AND JASON TUMLINSON^{3,4}

¹*Department of Astronomy, University of California, Berkeley, CA 94720*

²*Miller Institute for Basic Research in Science, University of California, Berkeley, CA 94720*

³*Space Telescope Science Institute, 3700 San Martin Drive, Baltimore, MD 21218*

⁴*Department of Physics & Astronomy, Johns Hopkins University, 3400 N. Charles Street, Baltimore, MD 21218*

⁵*Department of Computational Mathematics, Science, and Engineering, Department of Physics and Astronomy, National Superconducting Cyclotron Laboratory, Michigan State University*

⁶*Large Synoptic Survey Telescope, Tucson, AZ 85719*

Submitted to ApJ

ABSTRACT

The circumgalactic medium (CGM) of the Milky Way is mostly obscured by nearby gas in position-velocity space due to the location and motion of observers inside the Galaxy. While most studies on the Milky Way’s CGM to date focus on easier-to-detect high-velocity gas ($|v_{\text{LSR}}| \gtrsim 100 \text{ km s}^{-1}$), it only partially represents the entire CGM, resulting in substantial biases. Here we investigate four observational biases inherent in the studies of the Milky Way’s CGM with mock observations on a Milky-Way analog from the FOGGIE simulations. With a mock observer placed inside the simulated galaxy at off-center locations consistent with that of the Sun, we find that: (i) high-velocity-based studies could miss $\sim 2/3$ of the Milky Way’s CGM mass; (ii) once we correct velocities from the local standard of rest to the galaxy’s rest frame, gas infall rate (\dot{M}) for cold gas observable in H I 21cm emission is reduced from $-0.25 \text{ M}_{\odot} \text{ yr}^{-1}$ to $-0.05 \text{ M}_{\odot} \text{ yr}^{-1}$, while \dot{M} for gases at warmer phases are less affected; (iii) O VI and N V are likely to be good UV tracers of the Milky Way’s outer CGM ($r \gtrsim 15 \text{ kpc}$), whereas C IV maybe less sensitive; (iv) because of the clumpiness and radial distribution of CGM gas, the scatter in ionic column densities is a factor of 2 higher when the CGM is observed from the inside-out versus from external views. Our work highlights that observations of the Milky Way’s CGM, especially those using H I emission and UV absorption lines, are highly biased because we reside inside the Galaxy. We demonstrate that these biases can be quantified and calibrated through synthetic observations with simulated Milky-Way analogs.

Keywords: Circumgalactic medium(1879) – Milky Way Galaxy(1054) – High-velocity clouds(735) – Hydrodynamical simulations(767) – Spectroscopy(1558) – Quasar absorption line spectroscopy(1317)

1. INTRODUCTION

With an analogy borrowed from the Sun, Spitzer (1956) proposed that the Milky Way be surrounded by a hot corona in pressure equilibrium with cold dense gas seen in Ca II and Na I absorption lines (Münch & Zirin 1961). The hot corona, with temperature of tens

of thousands to millions Kelvin, should be detectable in ultraviolet (UV) absorption lines. Later on, Bahcall & Spitzer (1969) estimated a total mass of $\sim 3 \times 10^9 \text{ M}_{\odot}$ for extended halos of normal galaxies visible via such UV absorption lines. The hot corona or extended halo, now commonly referred to as the “gaseous halo” (Putman, Peek, & Joung 2012) or “circumgalactic medium (CGM)” (Tumlinson, Peebles, & Werk 2017), has been broadly studied in galaxies in local Universe as well as at higher redshifts. The CGM is a buffer zone that

Corresponding author: Yong Zheng
yongzheng@berkeley.edu

smoothly connects a galaxy’s interstellar medium (ISM) and the intergalactic medium. Its extent is loosely defined using the virial radius of a galaxy. The CGM is found to be multiphase and massive (Chen et al. 2010; Stocke et al. 2013; Werk et al. 2014; Borthakur et al. 2015; Lehner et al. 2015; Keeney et al. 2017; Prochaska et al. 2017), and with clumpy structures (Rubin et al. 2018; Lopez et al. 2018) and complex kinematics (Bordoloi et al. 2011; Nielsen et al. 2016; Ho et al. 2017; Lau et al. 2018; Martin et al. 2019). Beyond $L \sim L^*$ galaxy hosts, circumgalactic gas is also detected in low-mass dwarfs (Bordoloi et al. 2014; Liang & Chen 2014; Burchett et al. 2016; Johnson et al. 2017; Zheng et al. 2019b), star-bursting galaxies (Heckman et al. 2017), quasar (QSO) host galaxies (Johnson et al. 2015; Berg et al. 2018), and massive quiescent galaxies (Chen et al. 2018; Smailagić et al. 2018; Zahedy et al. 2019; Berg et al. 2019).

The Milky Way hosts a CGM broadly observed in wavelengths ranging from H I 21cm to UV and X-ray. In the following, we refer to the Milky Way’s CGM as those diffuse features beyond its interstellar medium (ISM) but not associated with the Magellanic Clouds, unless otherwise specified. In H I emission-line and UV absorption-line observations, the Milky Way’s CGM is studied in two velocity ranges: the high-velocity clouds (HVCs) at $|v_{\text{LSR}}| \gtrsim 90\text{--}100 \text{ km s}^{-1}$, and the intermediate-velocity clouds (IVCs) at $30\text{--}40 \lesssim |v_{\text{LSR}}| \lesssim 90\text{--}100 \text{ km s}^{-1}$, where v_{LSR} means the line-of-sight velocity with respect to observers at the local standard of rest (LSR). The distances to HVCs and IVCs can be determined using halo stars with known distances: for a pair of close stellar sightlines, if UV absorption lines are present in the further star but absent in the closer one, then the distance to an HVC or IVC is bracketed. With such a technique, HVCs are constrained to be at distances of $\sim 5\text{--}15 \text{ kpc}$ and IVCs at $\sim 0.5\text{--}2 \text{ kpc}$ (Schwarz et al. 1995; Wakker & van Woerden 1997; Wakker 2001; Wakker et al. 2007; Thom et al. 2008; Wakker et al. 2008). Other physical quantities of HVCs and IVCs follow subsequently as their distances are determined, such as cloud masses and gas infall rates, which we will discuss in detail in later sections (see §3.1, §5). We refer the reader to the book of “High-Velocity Clouds” by van Woerden et al. (2004) and other authors therein for detailed reviews on the historical developments and current studies of H I/UV HVCs and IVCs.

Unlike extragalactic CGM observations where only impact parameters and transverse velocities can be obtained, studies of the Milky Way’s CGM have the advantage to measure gases’ radial velocities, which are critical for accessing the role of CGM in replenishing the Milky

Way’s star-formation fuel (e.g., Wakker et al. 2008; Shull et al. 2009; Lehner & Howk 2011; Putman et al. 2012; Richter et al. 2017; Fox et al. 2019). However, that we reside inside the Milky Way’s ISM at an off-center location ($R_0 = 8.2 \text{ kpc}$, Table 1; see BG16) leads to many observational biases yet to be constrained. In this work, we aim to qualitatively address four biases plaguing the studies of the Milky Way’s CGM using synthetic observations of a Milky-Way analog selected from a cosmological hydrodynamical zoom simulation – Figuring Out Gas & Galaxies in Enzo (FOGGIE; Peebles et al. 2019; Corlies et al. 2018). Hereafter, we refer to this mock Milky Way and its related synthetic observations as the “Mocky Way.”

The first observational bias is related to the focus of studying the Milky Way’s CGM at high-velocity regime ($|v_{\text{LSR}}| \gtrsim 100 \text{ km s}^{-1}$). Because nearby ISM and IVC gas generally move at lower velocities (e.g., Wakker 1991; Wakker & van Woerden 1997; Wakker 2001; van Woerden et al. 2004; Savage et al. 2003; Savage & Wakker 2009; Wakker et al. 2012), observations of the Milky Way’s CGM mostly favor the high-velocity part of H I or UV spectra (e.g., Sembach et al. 2003; Lehner & Howk 2011; Lehner et al. 2012; Richter et al. 2017; Fox et al. 2019). Such HVC-based studies underestimate the total mass of the Milky Way’s CGM: as shown by Zheng et al. 2015, $\sim 50\%$ of the Milky Way’s CGM mass is likely to be neglected because of their lower velocities.

Secondly, radial velocities and distances measured for the Milky Way’s CGM gas are toward the LSR instead of the Galactic center, introducing a bias in calculating gas flow rates $\dot{M} \equiv Mv/d$, where M , v , and d denote gas mass, velocity, and distance. Depending on how v and d values are adopted, \dot{M} values differ among literature work and are often difficult to compare. The simplest method is to use v_{LSR} and distances with respect to LSR (d_{LSR}) directly, resulting in \dot{M}_{in} values biased toward observers at LSR (e.g., Wakker et al. 2007; Lehner & Howk 2011). Other methods involve: (i) correcting d_{LSR} to distance toward the Galactic center (d_{G} ; e.g., Richter et al. 2017); (ii) converting v_{LSR} to v_{GSR} to account for disk rotation (e.g., Fox et al. 2019); (iii) reconstructing true gas velocity vectors toward the Galactic center with assumptions on gas tangential velocities and 3-dimensional spatial distribution (e.g., Thom et al. 2008; Putman et al. 2012).

Thirdly, studies of the Milky Way’s CGM in UV absorption lines are biased toward nearby dense gas within $\sim 15 \text{ kpc}$ for their dominant absorption-line signals in QSO/stellar spectra (e.g., Lehner & Howk 2011; Lehner et al. 2012). The Milky Way’s outer CGM ($\gtrsim 15 \text{ kpc}$) has remained largely unattended to except the Magellanic

Clouds and their associated gaseous features (Putman et al. 2002; Stanimirović et al. 2008; Nidever et al. 2008; Richter et al. 2013; Fox et al. 2014). A general reasoning is that the outer CGM has too low density to manifest itself in QSO absorption lines. However, Zheng et al. (2019a) demonstrate that the Milky Way’s outer CGM is non-negligible in order to explain the distribution of Si IV column densities measured towards 132 QSOs across the sky (see also Qu & Bregman 2019). Lastly, because we observe the Milky Way’s CGM from the inside-out and are biased toward nearby gas, it remains difficult to directly compare the Milky Way’s CGM to extragalactic systems of $L \sim L^*$ galaxies.

The observational biases mentioned above can be addressed and quantified by analyzing simulated Milky-Way analogs with consistent observational setups, which is the motivation and goal of this work. We start in §2 with information on the FOGGIE simulation, including feedback recipe, code information, resolutions, etc. We proceed with analyses on the physical properties of the simulated halo in §3. We compare the simulated galaxy with the Milky Way and discuss their similarities and differences. In §4, we generate synthetic observations by putting a mock observer inside the simulated galaxy and building a galactic coordinate system consistent with that of the Milky Way. We show our results in §5 which quantifies the four observational biases inherent in the Milky Way’s CGM studies, and discuss advantages, caveats, and future directions of using FOGGIE simulations for Mocky Way analyses in §6. Lastly, we summarize in §7.

For consistency, throughout this work we will use the terminology as the following unless otherwise specified. (I) we define the CGM as *a space within the virial radius (R_{200}) of a galaxy but beyond the galaxy’s immediate ISM/disk region*. (II) *cold, cool, warm, and hot* gas are defined as those with temperature of $T < 10^4$ K, $10^4 \leq T < 10^5$ K, $10^5 \leq T < 10^6$ K, and $T \geq 10^6$ K, respectively, following the definitions in Tumlinson, Peebles, & Werk (2017). (III) we define *high-velocity* gas as that with velocities of $|v| > 100 \text{ km s}^{-1}$, and *low-velocity* gas with $|v| \leq 100 \text{ km s}^{-1}$, regardless of the rest frames (see next point). Note that, this definition of low-velocity gas includes those intermediate-velocity ($30 \lesssim |v_{\text{LSR}}| \lesssim 100 \text{ km s}^{-1}$) and low velocity ranges ($|v_{\text{LSR}}| \lesssim 30 \text{ km s}^{-1}$) commonly used in the literature. (IV) to discuss true velocity vectors pointing toward the galactic center, we use GRF to identify the galaxy’s rest frame. We emphasize that v_{GRF} is different from v_{GSR} – the latter means gas velocities v_{LSR} are corrected for disk rotation, but the corresponding velocity vectors are still projected toward observers at LSR.

2. SIMULATION SETUP

The simulation we analyze here is an updated version of the “high resolution” simulation of the Tempest halo first presented in Peebles et al. (2019) (hereafter Paper I). We briefly summarize the simulation setup here, focusing on the changes made since Paper I.

In brief, the FOGGIE simulations are cosmological hydrodynamic simulations evolved with the block-structured adaptive mesh refinement (AMR) code Enzo (Bryan et al. 2014; last described in Brummel-Smith et al. 2019) using a flat Planck Collaboration et al. (2014) Λ CDM cosmology ($1 - \Omega_\Lambda = \Omega_m = 0.285$, $\Omega_b = 0.0461$, $h = 0.695$) and a Piecewise Parabolic Method (PPM) hydro solver. The Tempest halo was selected to have a Milky Way-mass at $z = 0$ ($M_{\text{halo}} \simeq 1.5 \times 10^{12} M_\odot$; see §3 for more detailed galaxy and halo properties) and a relatively quiescent merger history at $z < 1$. The simulation domain is a $(100 h^{-1} \text{cMpc})^3$ box; the Tempest initial conditions were generated using the “cosmological zoom” method, with a 256^3 grid cell/particle base resolution and an effective resolution of $4,096^3$ particles ($M_{\text{dm}} = 1.39 \times 10^6 M_\odot$) in the region of interest, which is a Lagrangian region encompassing all of the particles within two virial radii of the galaxy at $z = 0$. We then evolved these zoom simulations on the NASA Pleiades supercomputer with a maximum of 11 levels of adaptive mesh refinement (cell sizes of $\simeq 190 \text{ pc}/h$ comoving) and 10 levels of forced (i.e, uniform) refinement (cell sizes of $\simeq 380 \text{ pc}/h$ comoving) within a $\pm 100 \text{ kpc}/h$ comoving box tracking the halo since $z = 6$ in order to ensure resolution of small spatial scales within the CGM.

Throughout we consider the output at $z = 0.102$ as this was the most recent output at the time of analysis. At $z = 0.102$, the ISM resolution is 249 physical parsec and the CGM resolution within the refined region is 498 physical parsec. As described in Paper I, the only feedback implemented is thermal feedback from supernovae.

We made two major changes to the setup presented in Paper I. First, we decreased the minimum mass at which stars can form from $2 \times 10^4 M_\odot$ to $1000 M_\odot$. This was motivated by finding that small halos at early times were not forming stars in the old simulation; the main impact of this change is an increase in early star and thus metal production. Second, we implemented self-shielding as a modification in the metagalactic UV background used by Grackle (Smith et al. 2017) when calculating cooling rates; this implementation is described in more detail in Emerick et al. (2018). As expected, this choice leads to higher H I column densities, especially at early times.

3. PROPERTIES OF THE SIMULATED GALAXY

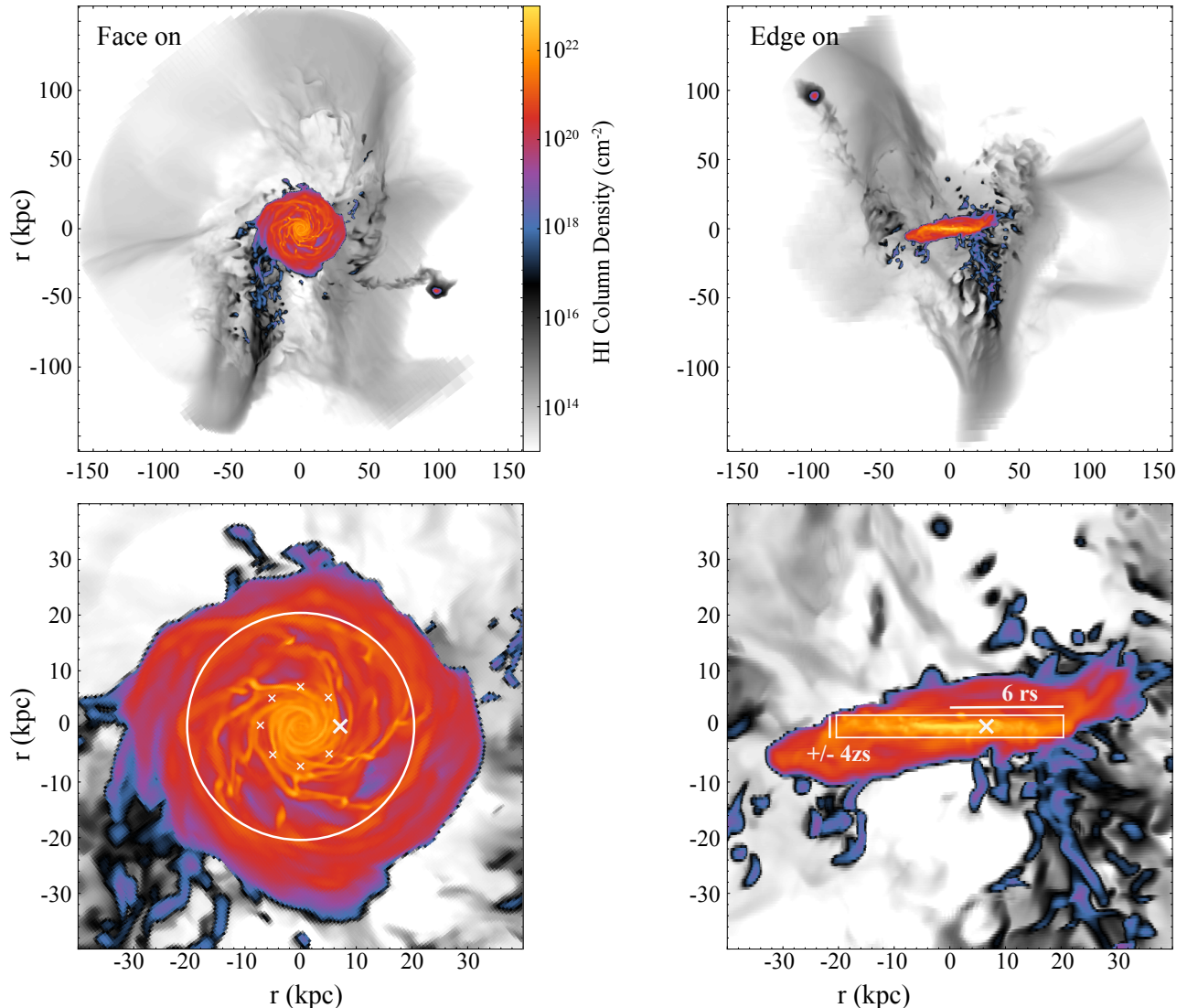


Figure 1. Face-on (left) and edge-on (right) projections of H I column density of Tempest at $z \simeq 0.1$. The top panels show H I distribution within the virial radius, whereas the bottom panels zoom into the inner 40 kpc regions to highlight the disk structures. The circle on the bottom left panel and the rectangle on the bottom right panel indicates the size of the cylindrical disk, with radius of $6r_s$ and height of $\pm 4z_s$. $r_s = 3.4$ kpc is the scale length of the H I disk and $z_s = 0.5$ kpc is its scale height. The fiducial off-center observer is placed at $2r_s$ in the disk plane (denoted with a thick cross), consistent with the position of the Sun in the Milky Way. We also select 7 other off-center locations (smaller crosses) 45° apart from each other at the same solar circle, which are used to study the variation due to observations at different locations. The color scheme in this figure is designed such that blue roughly reflects the N_{HI} detection limit of existing galaxy surveys at $N_{\text{HI}} \sim \text{a few} \times 10^{17-18} \text{ cm}^{-2}$ or higher (e.g., LAB, Kalberla et al. 2005; AGES, Auld et al. 2006; CHILES, Fernández et al. 2016; HI4PI, HI4PI Collaboration et al. 2016; GALFA-H I, Peek et al. 2018). Any structures with dark-grey colors may not be detected in current H I 21cm sensitivity.

In this section, we discuss the physical properties of the Tempest halo and galaxy at $z \simeq 0.1$. As we describe the physical properties, we compare them with those of the Milky Way (see Table 1) and comment on the similarities and differences.

3.1. Mass, Size, and Rotation Curve

In Figure 1, we display the face-on and edge-on projections of the H I column density (N_{HI}) of the galaxy. The galaxy’s virial radius ($R_{200} = 161.5$ kpc) is defined as the radius within which the mean density of dark matter and baryons is 200 times the critical density of the Universe at $z = 0.102$ based on cosmological parameters from Planck Collaboration et al. (2016). At this simulation output, the galaxy has evolved to redshift $z = 0.102$

Table 1. Galaxy Properties

Variable	Tempest	Milky Way
z	0.102	0.0
R_{200} (kpc)	161.5	211.6 ± 21.7^a
M_{200} (M_\odot)	0.49×10^{12}	$(1.1 \pm 0.3) \times 10^{12}, b$
$M_{\text{bary},200}$ (M_\odot)	8.38×10^{10}	$(8.5 \pm 1.3) \times 10^{10}, c$
$M_{*,200}$ (M_\odot)	5.37×10^{10}	$(5 \pm 1) \times 10^{10}, d$
R_0 (kpc)	6.8	8.2 ± 0.1^e
r_s (kpc)	3.4	$2.74\text{--}5.55^f$
z_s (kpc)	0.5	$0.08 - 0.22$ at $< R_0^g$
$M_{\text{hot halo}}$ (M_\odot)	$1.3 \times 10^{8,h}$	$(2.8 \pm 0.5) \times 10^{10}, i$
$M_{\text{HI HVC}}$ (M_\odot)	0.23×10^7 (1.3%) ^j	$2.6 \times 10^7, k$
$M_{\text{ionized HVC}}$ (M_\odot)	0.16×10^8 (46%) ^l	$1.1 \times 10^8, m$
$M_{\text{CGM,gas}}$ (M_\odot)	$1.19 \times 10^{10}, n$	N/A

NOTE— (a) virial radius (BG16). (b) total mass including baryons and dark matter. The quoted Milky-way value is a straight mean from halo stellar kinematic estimates compiled by BG16 in their table 8. (c) total baryonic mass, including stars and gas, within R_{200} (BG16). (d) total stellar mass within R_{200} (BG16). (e) weighted-mean by BG16 with a list of literature R_0 values compiled in their table 3. (f) Diplás & Savage (1991), see also Kalberla et al. (2007); Kalberla & Dedes (2008). (g) excluding the Galactic nuclear region, Lozinskaya & Kardashev (1963); Dickey & Lockman (1990); Putman et al. (2012). (h) total hot gas within R_{200} of the simulated CGM, excluding the disk. (i) hot halo gas ($T \gtrsim 10^6$ K) within 250 kpc from Bregman et al. (2018), estimated with a β -model density profile $n(r) \propto r^{-3/2}$ ($\beta \approx 0.5$). (j) cold, high-velocity gas in the CGM within 15 kpc, percentage in the parenthesis is the ratio of high-velocity cold CGM gas mass to the total cold CGM gas mass within 15 kpc. (k) see review by Putman et al. (2012). (l) same as j, but for cool and warm high-velocity gas. (m) Lehner & Howk (2011), ionized HVC, assuming ionized HVC covering fraction of 0.5, metallicity of $0.2 Z_\odot$, and distance of 12 kpc. (n) total amount of gas in the simulated CGM.

with a well-settled gaseous disk. The edge-on projection shows a thin gaseous disk with a large warp extending beyond the disk. Although we do not specifically study the gaseous warp in this work, we note that it is consistent with the Milky Way hosting a large extended warp detectable in H I 21cm emission line (Diplás & Savage 1991; Levine et al. 2006; Kalberla et al. 2007; Kalberla & Dedes 2008).

We define the disk as a cylinder at the galaxy center, as shown in the bottom panels of Figure 1. The radius of the disk cylinder is taken as 6 times the scale length of the disk (r_s) and its thickness ± 4 times the scale height (z_s), which are decided by examining the edge-on projection of the galaxy in Figure 1 and ensure

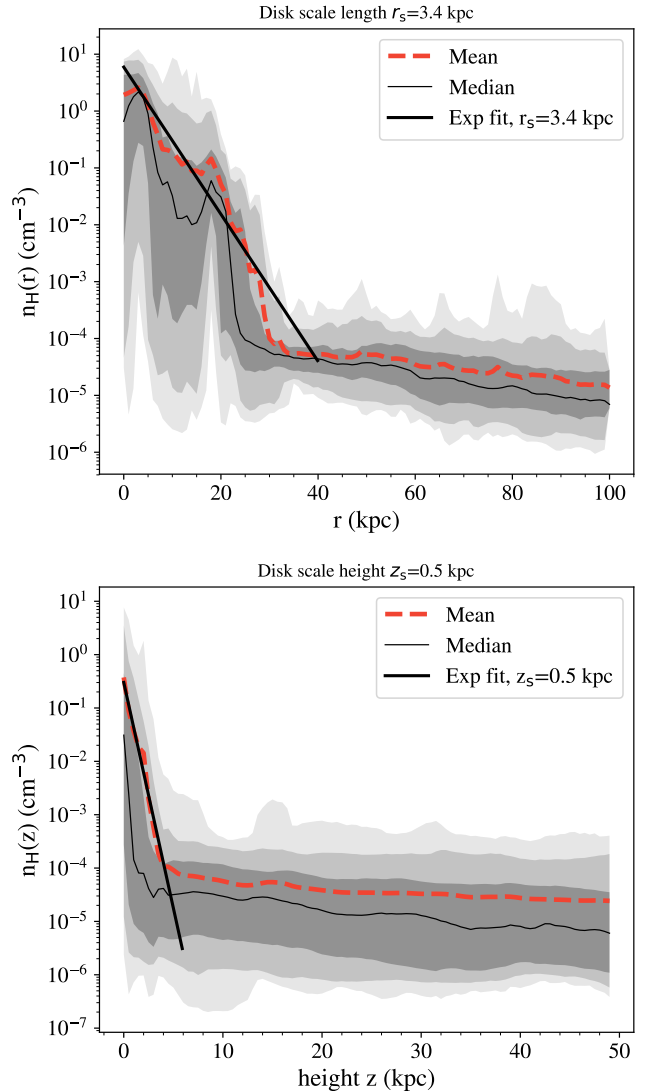


Figure 2. **Top:** hydrogen (H) radial density profile in the disk. The red dashed line shows the mean n_{H} value in each r bin and the thin black curve indicates the median value. The heavy, median, and light grey shades show the 3σ (99.7%), 2σ (95.5%), and 1σ (68.3%) confidence levels, respectively. We fit an exponential profile for mean $n_{\text{H}}(r)$ within 25 kpc and find a disk scale length of $r_s = 3.4$ kpc, which is consistent with the Milky Way’s H I disk value ($r_s=3.75$ kpc; Kalberla & Dedes 2008). **Bottom:** n_{H} along the z direction perpendicular to the disk plane. Similarly, we find a scale height of $z_s = 0.5$ kpc, which is thicker than the thickness of the Milky Way’s H I disk ($\sim 80\text{--}220$ pc) within the solar circle. Given the resolution of the simulation, we consider r_s well resolved but not z_s . See §3.1 for details.

the cylindrical region encloses the flat part of the thin gaseous disk structure. As we are interested in the gas in the vast volume of the galaxy’s CGM, the choice of the disk cylinder size does not affect our analyses and conclusion significantly. We calculate the disk scale length

r_s and scale height z_s by fitting exponential functions $n(x) = n_0 e^{-x/x_s}$ to the mean hydrogen radial and vertical density profiles, where x stands for r or z (see Figure 2). We find $r_s = 3.4$ kpc, consistent with the scale length derived for the Milky Way’s H I disk beyond $\gtrsim 10$ kpc (e.g., $r_s = 2.74 - 5.55$ kpc by [Diplas & Savage 1991](#); $r_s = 3.75$ kpc by [Kalberla & Dedes 2008](#)). The scale height of the disk is $z_s = 0.5$ kpc. Because the cell size of the simulation is 0.25 kpc, we consider the scale radius r_s of the disk well resolved but not the scale height z_s , which is one of the caveats we discuss in §6. It is noteworthy that the thickness of the Milky Way’s H I disk within the solar circle is 80–220 pc except near the Galactic nucleus region ([Lozinskaya & Kardashev 1963](#); [Dickey & Lockman 1990](#); [Putman et al. 2012](#)), which means the simulation is producing reasonable characteristic scale values at its current resolution.

Overall, we find a total mass of $M_{200} = 0.49 \times 10^{12} M_\odot$ for dark matter and baryons in the simulated galaxy within R_{200} , of which 83.0% (by mass) is dark matter, 10.9% is stars, and the rest 6.1% is gas. For references, current estimates of the total mass of the Milky Way within its virial radius range from $5.5 \times 10^{11} M_\odot$ to $2.6 \times 10^{12} M_\odot$ (e.g. [Gibbons et al. 2014](#); [Watkins et al. 2010, 2019](#)) with a typical mean value at $(1.1 \pm 0.3) \times 10^{12} M_\odot$ ([BG16](#)). The simulated galaxy is at the lower bound of the Milky Way literature values. We further calculate the masses of some particular CGM gas components for a rough comparison with the Milky Way’s values, and tabulate our result in Table 1. We find that the hot gas mass in the simulated CGM is two orders of magnitude lower than that estimated for the Milky Way ([Bregman et al. 2018](#)). The cold high-velocity gas (equivalent to H I HVCs) and cool-warm high-velocity gas (equivalent to ionized HVCs) are an order of magnitude less massive than their corresponding observational values. Overall, the simulated galaxy does not produce as much CGM gas as the Milky Way (see also §4 and §6).

When compared to existing surveys on $L \sim L^*$ galaxies at $z \sim 0.1 - 0.2$, we find that the simulated galaxy is among the most abundant galaxy types and masses (e.g., [Chen & Mulchaey 2009](#); [Prochaska et al. 2011](#); [Werk et al. 2013](#); [Tumlinson et al. 2013](#); [Stocke et al. 2013](#); [Borthakur et al. 2015](#); [Burchett et al. 2019](#)). In Figure 3, we split the simulated CGM gas into cold, cool, warm, and hot phases. As these masses are difficult to robustly constrain empirically, here we only aim for an order-of-magnitude comparison with observations to evaluate if the simulated CGM is representative for $L \sim L^*$ galaxies. We find that the cool-warm phase gas in the simulated CGM is $\sim 6.5 \times 10^9 M_\odot$, which is about a factor of 2 less massive than the observation values

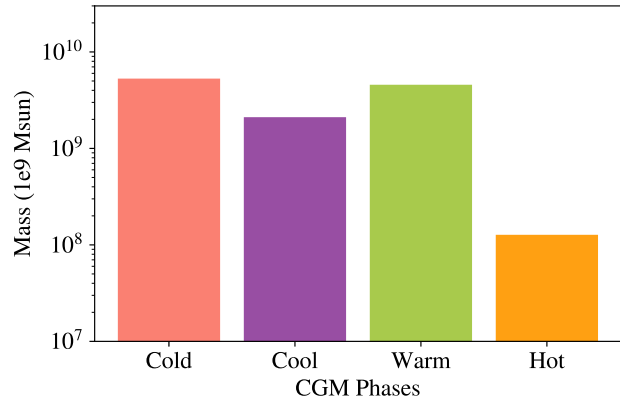


Figure 3. Masses of cold, cool, warm, and hot CGM gases within R_{200} . The masses of the cold, cool, warm and hot phases are $5.2 \times 10^9 M_\odot$, $2.1 \times 10^9 M_\odot$, $4.5 \times 10^9 M_\odot$, and $1.3 \times 10^8 M_\odot$, respectively. In general, we find that the total CGM mass at cool/warm phases is a factor of two less than those estimated in extragalactic studies.

($\sim 10^{10-11} M_\odot$ for cool-warm CGM gas at $T \sim 10^{4-5.5}$ K; e.g., [Chen et al. 2010](#); [Tumlinson et al. 2011](#); [Werk et al. 2014](#); [Lehner et al. 2017](#); [Prochaska et al. 2017](#); [Keeney et al. 2017](#); [Bregman et al. 2018](#); [Lehner et al. 2020](#), in prep).

Lastly, we check the galaxy’s rotation curve of the simulated galaxy in Figure 4. The circular velocity is calculated as $v_c \equiv \sqrt{GM(< R)/R}$, where $M(< R)$ is the total dark matter and baryonic mass enclosed within radius R . We follow the method in [El-Badry et al. \(2018\)](#) and define the rotation velocity v_{rot} as the gas-mass-weighted mean azimuthal velocity v_ϕ per radial bin, where $v_\phi \equiv (xv_y - yv_x)/\sqrt{x^2 + y^2}$. In this calculation, \vec{z} is along the angular momentum direction, \vec{x} is the direction from the galaxy center to the fiducial off-center observer, and \vec{y} follows the right-handed rule. The velocity dispersion σ_v is mass-weighted standard deviation of v_ϕ values per radial bin. In general, v_{rot} matches v_c , suggesting that gas in the simulated galaxy is rotationally supported. When comparing to the Milky Way’s rotation curve, We find that the galaxy’s v_{rot} is consistent with the Milky Way’s values at $R \gtrsim 5$ kpc ([Bland-Hawthorn & Gerhard 2016](#); also see [Sofue et al. 2009](#); [Koposov et al. 2010](#); [Kafle et al. 2012](#); [Reid et al. 2014](#); [López-Corredoira 2014](#); [Küpper et al. 2015](#)).

3.2. Phases, Kinematics, and Morphology

Before we mock up observations to investigate how the Milky Way’s CGM studies are biased, we outline the physical properties of the simulated CGM to form a baseline. In this section, we study gas inflows and outflows in the simulated galaxy, with velocity defined with respect to the galaxy center, i.e., the galaxy’s rest

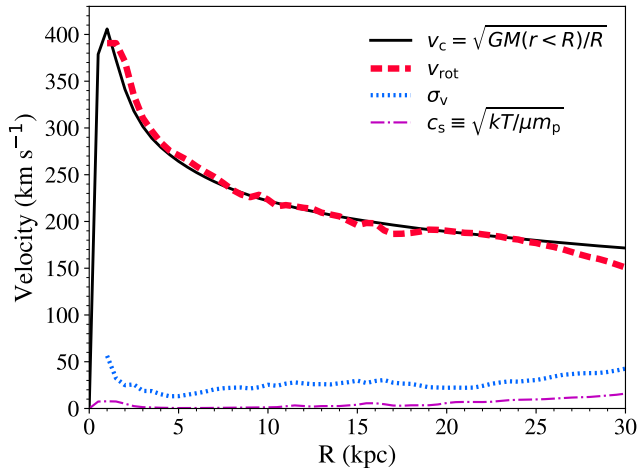


Figure 4. Circular velocity v_c , mass-weighted gas rotation velocity v_{rot} , velocity dispersion σ_v , and mass-weighted sound speed c_s of the simulated galaxy. We find that gas in the simulated galaxy is fully rotationally supported, and v_{rot} is largely consistent with the Milky Way values at $R > 5$ kpc.

frame (GRF). In GRF, v_r is the radial velocity component. We broadly define *inflows* as any CGM gas with $v_r < 0$ km s⁻¹, and *outflows* with $v_r > 0$ km s⁻¹, which likely include local motions such as turbulence and convection (Ford et al. 2014). We focus on the bulk properties (e.g., phases, kinematics, spatial distributions, and morphology) of inflows and outflows, but refrain from scrutinizing every interesting detail that arises. Investigations dedicated to analyzing the velocity structures (e.g., turbulence, convection) of the CGM with FOGGIE simulations are forthcoming.

In Figure 5, we show the phase diagrams and edge-on projections of outflows. The dense ($n_{\text{H}} \gtrsim 10^{-3}$ cm⁻³) and cold ($T \lesssim 10^4$ K) gas is mostly from the gaseous disk and warp, which we do not include in following discussion. In panel (a), we find that within each 10 kpc radial bin, outflowing gas remains in thermal pressure equilibrium and the pressure drops toward larger radii, in broad agreement with the radial pressure profile in Voit et al. (2019); similar radial pressure profile can be seen in inflows in Figure 6. However, the similar pressure gradients on the phase diagrams do not mean that inflows and outflows are well mixed, which can be easily seen by comparing their distinct morphology in panel (c) of both figures. Instead, the pressure gradient raises a question: is the gas (both inflows and outflows) in local pressure equilibrium?

Analyzing a suite of idealized simulations (Fielding et al. 2017), Lochhaas et al. (2019) find that the CGM in a high-mass halo ($M_{\text{h}} = 10^{12} M_{\odot}$) is dominated by thermal pressure and maintains pressure equilibrium in

most part of the halo. However, for a low-mass halo with $M_{\text{h}} = 10^{11} M_{\odot}$, thermal and non-thermal pressure (e.g., ram pressure and turbulence) plays equally important role in regulating dynamical status of the CGM gas. In their low-mass halo, the combination of thermal and non-thermal pressure is still not enough to support against gravity, suggesting that the CGM gas is not in dynamical equilibrium. Given the mass of the simulated galaxy we analyze, its CGM is likely to be in the middle of these two cases, where thermal pressure may play the major supporting role while non-thermal pressure is also non-trivial. However, these results are based on a spherically symmetric CGM lacking the cosmological accretion and mergers that likely affects the thermal and non-thermal pressure. Though the question of local pressure equilibrium is beyond the scope of this paper, it thus merits more a detailed investigation and will be examined in forthcoming FOGGIE analyses.

We proceed with panel (b) in Figure 5, which shows that outflowing gas exhibits a clear velocity gradient. Slower outflows are cooler and denser. We do not expect these slower outflows come from material cooling out of hotter medium, in which scenario both cool and hot gas should move at similar velocities (Li & Bryan 2014; Thompson et al. 2016; Schneider et al. 2018), thus no significant velocity gradient should exist. Instead, the slow and fast outflows occupy different volume space as shown in the edge-on projections in Panel (c)–(e). Fast outflows form large-scale bipolar structures, rushing out of the disk along perpendicular directions. They are metal-enriched ($Z \sim 0.1\text{--}1.0Z_{\odot}$) and hot ($T \gtrsim 10^6$ K). Conversely, slower outflows ($0 < v \lesssim 60$ km s⁻¹) occupy a much bigger volume, but are cooler ($T \lesssim 10^6$ K) and mostly metal-poor ($Z \lesssim 0.1 Z_{\odot}$). These slow outflows may not be directly related to feedback material from the galaxy to the CGM; instead, they may be related to local motions, such as convection and turbulence, that result in positive velocity signs (Ford et al. 2014). We further note that outflows are distributed in bipolar manner along the galaxy’s minor axis, consistent with galactic wind morphology observed in star-forming galaxies (e.g., Bland & Tully 1988; Veilleux et al. 2005), consistent with the hypothesis that such outflows produce excess in ionic equivalent width measured along the minor axes (Bordoloi et al. 2011; Kacprzak et al. 2012; Lan & Mo 2018; Martin et al. 2019), and simulations of galactic outflows (Li et al. 2017; Schneider et al. 2018; Nelson et al. 2019).

In Figure 6, we find that inflowing gas with $v_r < 0$ km s⁻¹ shows a similar radial density gradient on the phase diagram (panel a) as that of outflows. Faster inflows form large-scale filamentary structures, and

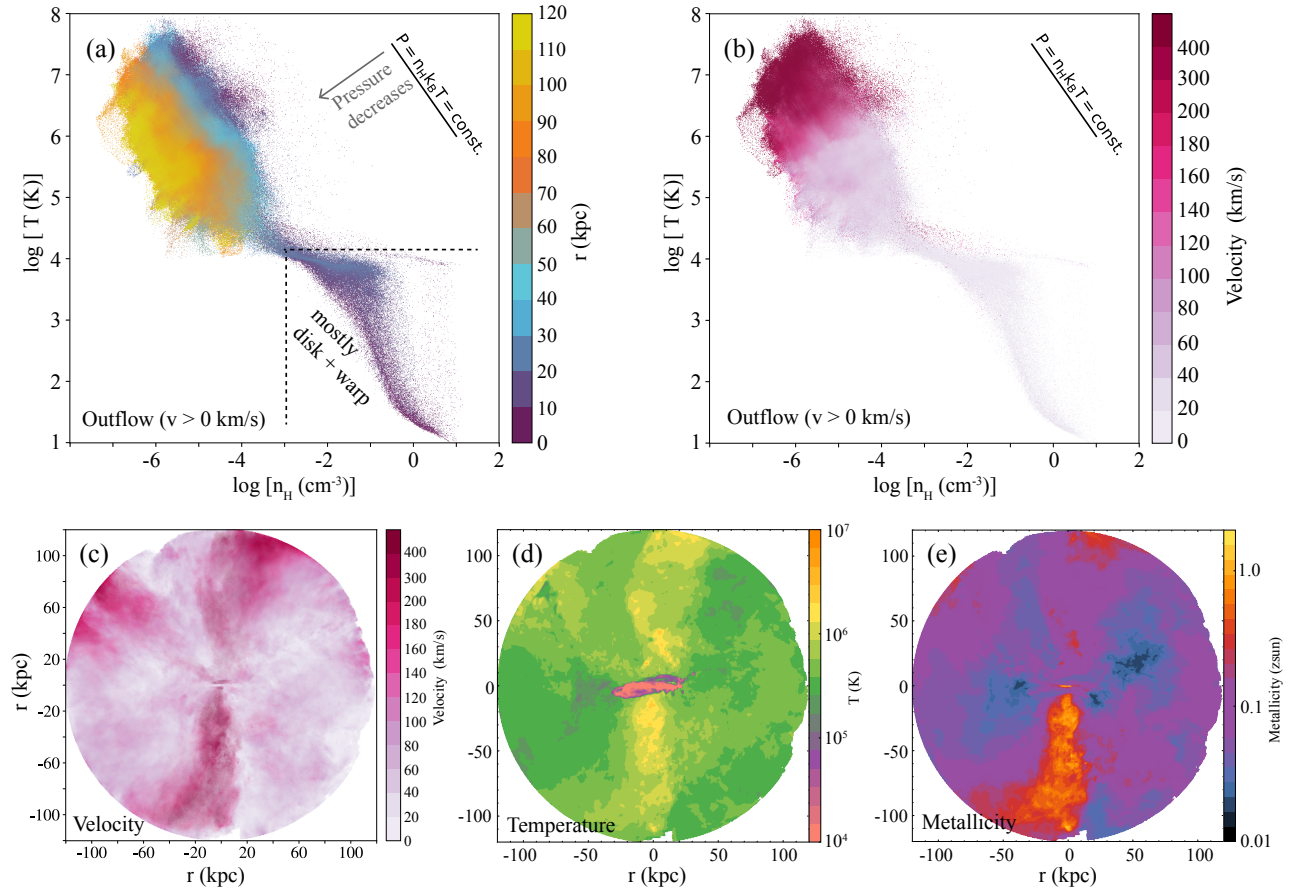


Figure 5. Outflows diagnosis ($v_{\text{GRF}} > 0 \text{ km s}^{-1}$). Panels (a) and (b) show phase diagram color-coded with radius and velocity with respect to the galaxy center. Panels (c), (d), and (e) show edge-on projections of outflow radial velocities (v_r), density-weighted temperature, and density-weighted metallicity, respectively. In panel (a), due to illustration effect, data points from larger radius bins are over-plotted on top of those from smaller radii, therefore the pressure spread within individual radius bins appear narrower. Overall, gases at fixed radii remain in local thermal pressure equilibrium. The thermal pressure gradually drops at larger radii as indicated by a gray arrow. In panel (b), outflow velocity exhibits a velocity gradient, with slower outflow being cooler and denser, regardless of the radius of the outflow. The correlation of outflow phase and velocity can also be spatially recognized in panels (c)-(e), with faster outflows on larger scale, more collimated (bipolar), and with higher temperature ($T \gtrsim 10^6 \text{ K}$) and metallicity (Z from ~ 0.1 to $> 1 Z_{\odot}$). Slower outflows fill more volume with lower temperature and metallicity. The spatial and kinematic distribution of outflows are in stark contrast with those of inflows as shown in Figure 6. See §3.2 for details.

are generally found at cooler phases except near the disk/warp region. The low metallicity ($Z \sim 0.01 Z_{\odot}$) gas of this fast-moving material shows that they are relatively pristine material from the intergalactic medium. On the other hand, slower inflows are more metal enriched. In panel (c), we see that these fast inflows make their way to the vicinity of the galaxy disk. However, as they approach the disk-halo interface of the galaxy within $\sim 10 \text{ kpc}$, gas temperature and metallicity become indistinguishable with ambient medium, indicating mixing with turbulence possibly playing a role. In §5, we show that the knowledge of these radial inflow/outflow structures and gas density distributions

is critical in understanding the observational biases in the Milky Way’s CGM studies.

4. SETUP OF SYNTHETIC OBSERVATIONS

Here we start with building a coordinate system in the simulated galaxy similar to that of the Milky Way’s Galactic coordinate system. We select eight off-center locations to place the mock observer, which are shown as crosses in the bottom panel of Figure 1. The off-center locations are 6.8 kpc away from the galaxy center, which is twice the disk scale length as informed based on the location of the Sun in the Milky Way. Among the eight locations, we randomly choose one as the fiducial off-center location (thick white cross in Figure 1) and

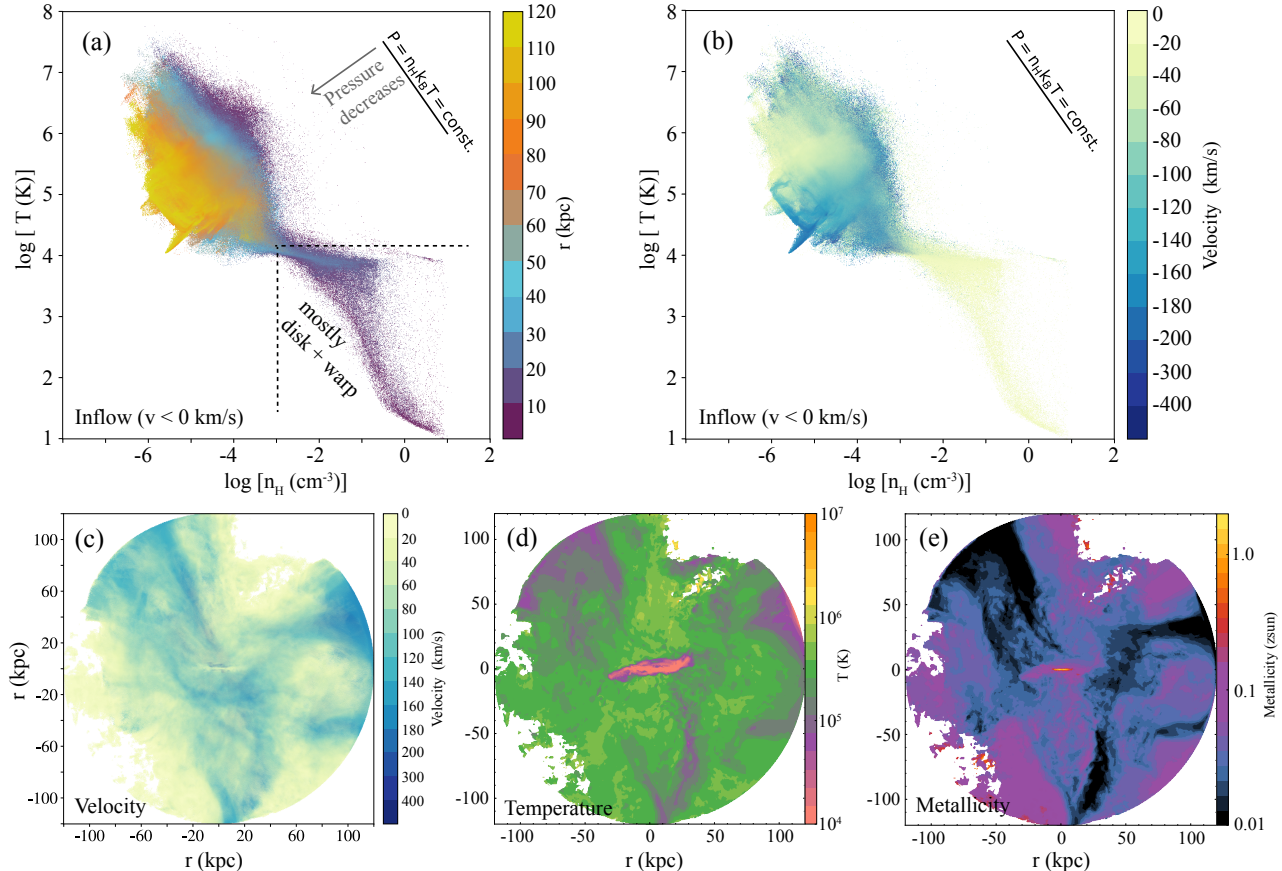


Figure 6. Inflows diagnosis ($v_{\text{GRF}} < 0 \text{ km s}^{-1}$), with figure legends similar to Figure 5. In panel (a), we observe a similar radial pressure gradient on the phase diagram as that of outflows in Figure 5. In panel (b), we do not find correlation between inflow velocities and phases, which is different from that of outflows. Panels (c)-(e) show that fast inflows form large-scale filamentary structures with low temperature ($T < 10^5 \text{ K}$) and metallicity ($Z \lesssim 0.01 Z_{\odot}$). When compared to Figure 5, we find that the fast inflows bypass the fast bipolar outflows. Slower inflows fill most of the volume of CGM and exist co-spatially with slower outflows, which suggest that these slower inflows and outflows may have different dynamical origins than their fast, large-scale counterparts. See §3.2 for more detailed discussion.

refer to it as needed in the following. We define the mock galactic longitude ℓ and latitude b in a consistent way as those of the Milky Way. Standing at an off-center location, the mock observer will find the galaxy center at $(\ell = 0^\circ, b = 0^\circ)$ and the anti-center at $(\ell = 180^\circ, b = 0^\circ)$; ℓ increases in a counter-clockwise manner when looking down from the north galactic pole, where north is defined as the direction of the disk’s angular momentum. b is positive above the galaxy plane and negative below. We calculate the bulk velocity of gas within 1 kpc of the mock observer and adopt it as the local standard of rest (LSR).

In Figure 7, we show how the all-sky distribution of H I column density (N_{HI}) changes as the mock observer moves from the galaxy center (top panel) to the fiducial off-center location (middle panel). Results from the other 7 off-center locations are similar, with gas structures observed at different ℓ because of the shifts of the

coordinate systems along the solar circle. Standing at the galaxy center (top panel), the disk appears flat with small cloud clumps and filaments extending beyond the disk plane. However, at the fiducial off-center location, we find that both the simulated disk and the extraplanar H I structures are reshaped. The disk remains relatively flat and thin within $\ell = \pm 90^\circ$ — this transformation is due to the mock observer moving away from the galactic center. Toward the outer galaxy, observers’ lines of sight go through less dense regions and the disk becomes more fluffy with a large warp (see Figure 1), which results in large flaring at $|\ell| > 90^\circ$.

As a sanity check, we show the Milky Way’s N_{HI} all-sky distribution from the HI4PI survey (HI4PI Collaboration et al. 2016) in the bottom panel. The N_{HI} values are integrated from $v_{\text{LSR}} = -600 \text{ km s}^{-1}$ to 600 km s^{-1} . When comparing the middle and bottom panels, we find that the simulation is unable to produce as much H I as

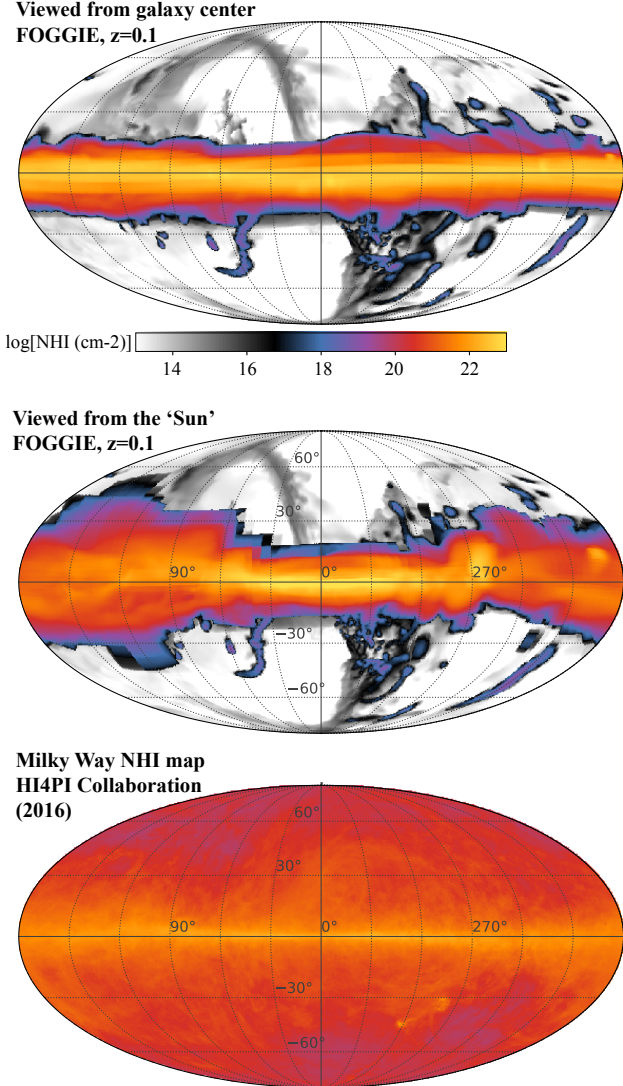


Figure 7. All-sky mollweide projection of N_{HI} . **Top:** N_{HI} seen by an observer at the center of the simulated galaxy. All three maps share the same color bar. **Middle:** N_{HI} seen by the fiducial off-center observer placed by a similar location as the solar system in the Milky Way plane. **Bottom:** the Milky Way’s H I 21cm emission within $\pm 600 \text{ km s}^{-1}$ of LSR observed by HI4PI Collaboration et al. (2016). We find that, (1) at $|b| \gtrsim 20^\circ$, the simulated galaxy does not produce as much H I as the Milky Way, and (2) along the galactic plane at $|b| \lesssim 20^\circ$, the simulated galaxy reaches similar column densities and structures as the Milky Way. Two reasons may be responsible for the discrepancy and similarity in N_{HI} allsky distribution. First, the simulated CGM is likely to be warmer than the Milky Way’s CGM thus most of its hydrogen is ionized. Second, the disk gravitational potential along z direction is not well resolved in FOGGIE, therefore, gas distribution at higher b is incorrect. See §4 for more details.

the Milky Way at higher Galactic latitude ($|b| \gtrsim 20^\circ$), suggesting that the simulated CGM is likely to be too warm thus too much of the hydrogen remains ionized. In addition, the low N_{HI} values are likely to be due to the fact that the thickness of the galaxy’s disk is not well resolved in the simulation (see §3.1), therefore the gravitation potential, thus the gas distribution, along the z -direction is incorrect. On the other hand, we find that the simulated galactic plane at $|b| \lesssim 10^\circ$ reaches a similar level of N_{HI} values as the Milky Way. And the disk starts to flare around $l = 90^\circ$ and 270° (middle panel), consistent with similar features in the Milky Way due to the Galactic warps (Diplas & Savage 1991; Levine et al. 2006; Kalberla et al. 2007; Kalberla & Dedes 2008).

The direct comparison with the HI4PI data also reveals the limitation of current FOGGIE simulations (as well as other cosmological zoom simulations). The HI4PI map shows very detailed H I structures all over the sky down to its resolution limit (16 arcmin; HI4PI Collaboration et al. 2016). Additionally, sharper H I fiber structures are revealed by the GALFA-H I data (4 arcmin; Clark et al. 2014; Peek et al. 2018) as well as other compact cloud clumps (e.g., Putman et al. 2002; Saul et al. 2012). Conversely, the middle panel shows smooth H I disk and warps, indicating the ISM in the simulated galaxy is not well resolved and not suitable for detailed analysis. Therefore, we only focus on the CGM part of the simulation which is beyond the designated cylindrical disk and within the galaxy’s virial radius.

5. RESULTS: QUANTIFYING OBSERVATIONAL BIASES

The purpose of this work is to identify and quantify observational biases plaguing the studies of the Milky Way’s CGM. We illustrative four biases in Figure 8 and address them in details in §5.1–5.4. We caution that the statistics we provide here are subject to the difference between the simulation and the Milky Way. Therefore, our result should be read as a qualitative assessment of the biases, with more work to be done in the future to systematically calibrate the biases.

5.1. Observational Bias I:

how much CGM gas is hidden at low velocity?

As illustrated in the spectral panel in Figure 8, in a UV absorption line spectrum, only the high-velocity ($|v_{\text{LSR}}| \geq 100 \text{ km s}^{-1}$) part of the spectrum is available to study the Milky Way’s CGM. Gas at low velocities is hidden behind nearby ISM material. Here we revisit the analysis conducted in Zheng et al. (2015) about the CGM mass distribution in the high-velocity observable regime and the low-velocity ($|v_{\text{LSR}}| < 100 \text{ km s}^{-1}$)

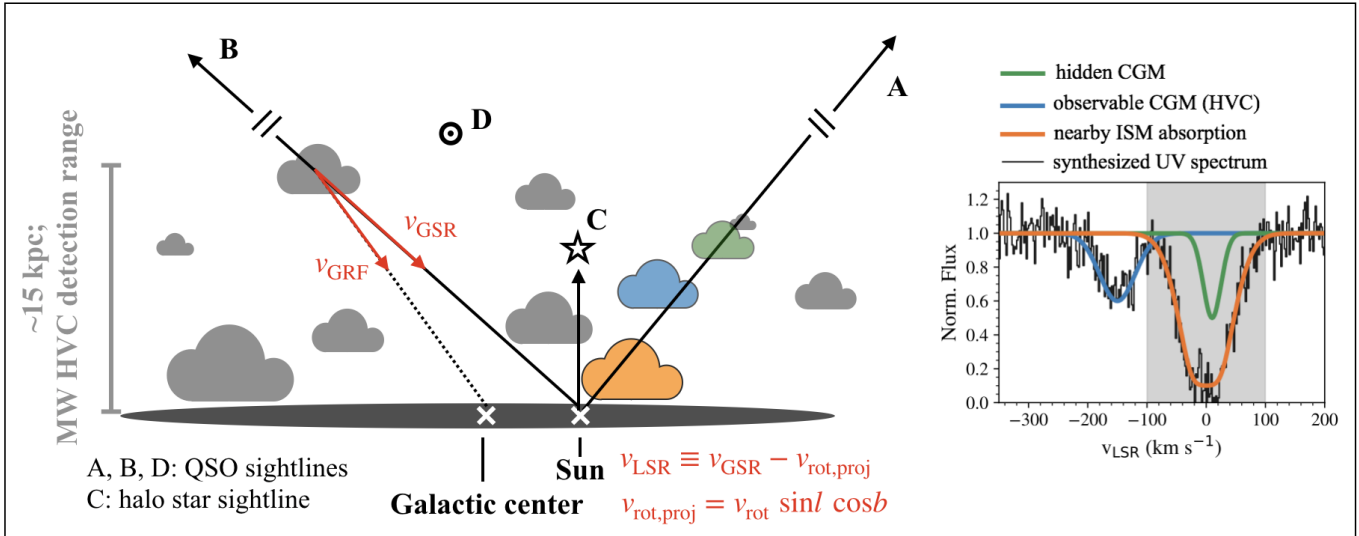


Figure 8. Cartoon illustration of four observational biases inherent in the Milky Way’s CGM studies. **Bias I** (§5.1): along sightline A, we revisit the question asked by Zheng et al. (2015) and estimate the fraction of CGM mass missing from high-velocity-based studies. As shown in the spectral panel, only the high-velocity portion of an absorption-line spectrum is available to study the Milky Way’s CGM. Gas at low velocities is hidden behind saturated absorption lines from nearby ISM, thus eluding the detection. **Bias II** (§5.2): along sightline B, we show that estimates of gas infall rates in the Milky Way could be highly biased because the velocity vectors are toward the Sun instead of the Galactic center. **Bias III** (§5.3): combining sightline A (QSO) and C (halo star), we investigate whether QSO absorption lines are sensitive enough to probe the Milky Way’s outer CGM beyond ~ 15 kpc and which ions are the best tracers. **Bias IV** (§5.4): we look into the difference between the Milky Way’s CGM (inside-out views; e.g., sightline A, B, C) and those of extragalactic systems (external views; e.g., sightline D), and investigate how the differences are related to the CGM’s gas structures.

hidden regime. Figure 9 shows the mass distribution measured in LSR frame (dotted lines and color shading). Averaging over the values from the eight off-center observing locations (see Figure 1), we find that the CGM mass hidden at low velocities is $f_{\text{hidden}} \equiv \frac{M(v_{\text{LSR}} < 100 \text{ km s}^{-1})}{M_{\text{all}}} \approx 2/3$, echoing Zheng et al’s result. When breaking the CGM gases into different phases, the f_{hidden} value for cold gases is the highest ($\sim 85\%$), while for gases at cool, warm, and hot phases, f_{hidden} is close to $\sim 50\%$.

5.2. Observational Bias II:

Velocity Rest Frames: v_{GRF} , v_{GSR} , and v_{LSR}

For the Milky Way observations, we are unable to obtain direct measurements of gas motions (e.g., velocity and mass flux rates) because gas velocities and distances are measured toward the Sun instead of the Milky Way center. As illustrated in sightline B in Figure 8, the velocity vectors thus mass flow rates are calculated with respect to local observers at LSR. Even if we convert v_{LSR} to v_{GSR} to correct for the disk rotation (e.g., as adopted in Fox et al. 2019), the velocity vectors are pointed still toward the LSR, while true velocity values cannot be recovered owing to our ignorance of gas tangential motions perpendicular to the lines of sight (see Thom et al. 2008; Putman et al. 2012).

To illustrate how observing rest frames affect observable quantities of the CGM gas, in Figure 9, we examine the mass distribution as a function of velocity measured in the galaxy’s rest frame (GRF, solid line) with those measured in the LSR (dotted line and shading). We find that the masses of cold, cool, and warm gases are more broadly distributed at higher velocities in the LSR than in the GRF. This is because the mock observer at the LSR is co-rotating with the disk, contributing additional velocity components along the lines of sight (Wakker 1991). The disk rotation affects gas at low Galactic latitudes the most, where add-on velocity due to observer’s co-rotation is the maximum. This is consistent with H I 21cm observation of the Milky Way, where we see gas moves at fast v_{LSR} along $l \pm 90^\circ$ where the contribution from rotation to the line-of-sight velocity is the maximum (Wakker 1991; van Woerden et al. 2004; Kalberla & Dedes 2008). On the other hand, the hot gas distribution varies little between the GRF and the LSR because these gas mostly distributes biconically at high galactic latitudes (see Figure 5), thus there is little contribution from the disk rotation when switching observing rest frames.

We further compare the mass flow rates (\dot{M}) of the CGM gas measured in the GRF and the LSR. We define $\dot{M} \equiv \Sigma M_i v_i / D_i$, where M_i , v_i , and D_i denote the

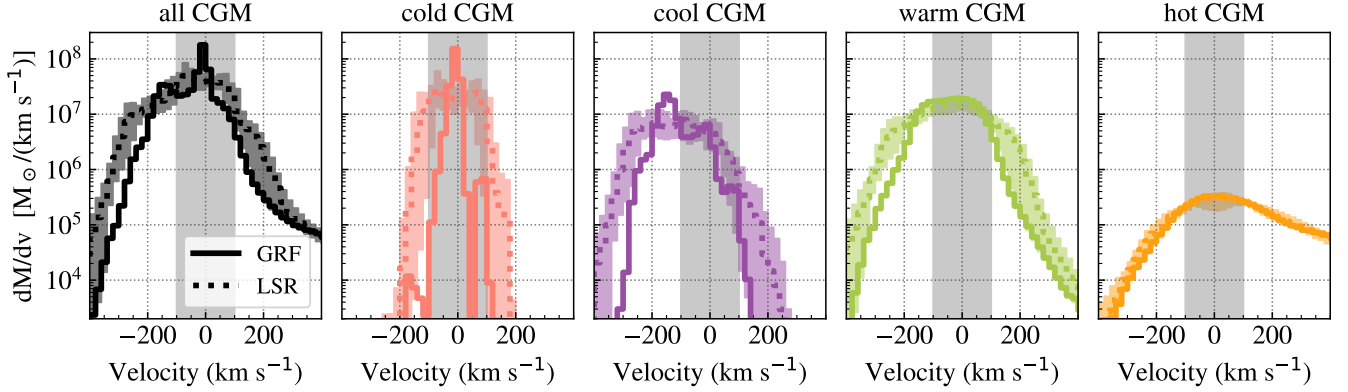


Figure 9. Gas mass as a function of velocity for all, cold, cool, warm, and hot CGM gas within R_{200} . Solid lines are quantities calculated in the GRF. Dotted lines and color shading are calculated with respect to off-center observers at the LSR: the dotted lines show values averaged over the eight off-center locations (see Figure 1), and the color shadings indicate the minimum and maximum value ranges. Vertical grey shades indicate the low-velocity spectral region less favorable in the Milky Way’s CGM studies because of contamination from nearby ISM. We find that: (i) on average $\sim 2/3$ of the CGM mass is hidden at low velocities, thus eluding detection (§5.1); (ii) CGM gases are dominantly infalling in cool and warm phases; (iii) when switching from the GRF to the LSR, cool and warm gas masses are redistributed to higher velocities due to the disk rotation (§5.2).

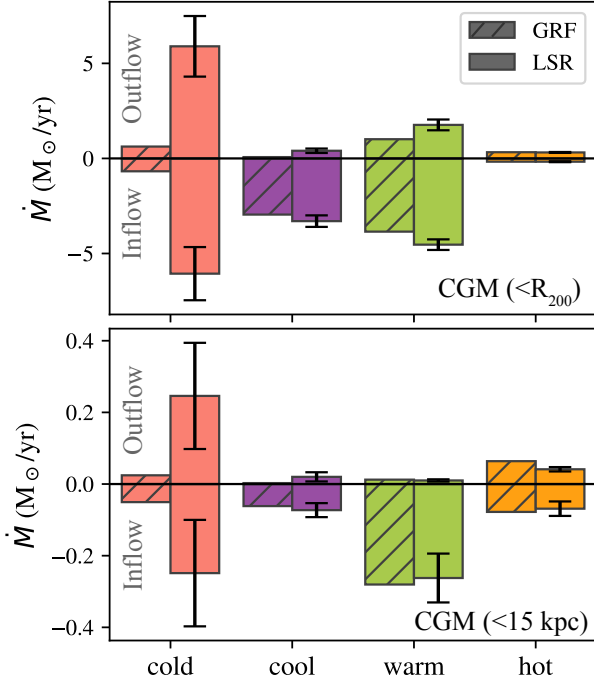


Figure 10. Inflow (\dot{M}_{in}) and outflow (\dot{M}_{out}) rates measured in the GRF (hatched) and the LSR (solid). The top panel shows \dot{M} for the entire CGM, whereas the bottom one is for the CGM gas with 15 kpc to compare with the Milky Way values. Each bar indicates the value averaged over the eight off-center locations (see Figure 1), and its error bar denotes 1σ value. Both panels show: (i) cool and warm CGM gases are dominantly infalling, while the net flow rates for cold and hot gases are not significant (see also Figure 9); (ii) when switching from the GRF to the LSR, \dot{M}_{in} and \dot{M}_{out} for the cold gas change by a factor of ~ 10 , while the values for gas at warmer phases do not change significantly.

mass, line-of-sight velocity, and distance of a given gas cell toward the mock observer. This definition of \dot{M} is widely used in studies of gas inflows and outflows (e.g., Lehner & Howk 2011; Putman et al. 2012; Rubin et al. 2014; Zheng et al. 2017; Bordoloi et al. 2017; Fox et al. 2019). In Figure 10, we show the mass flow rates of the inflows ($\dot{M}_{\text{in}} = \dot{M} < 0$) and outflows ($\dot{M}_{\text{out}} = \dot{M} > 0$) for the entire CGM gas (top panel) and for CGM within 15 kpc to compare with the Milky Way values (bottom panel). \dot{M} measured in the GRF (hatched regions) indicates true mass flow rates with respect to the galaxy center. The top panel shows that cool and warm gases are dominantly infalling, with a net flow rate of $\dot{M}_{\text{cool+warm}}^{\text{GRF}} = \dot{M}_{\text{in}}^{\text{GRF}} + \dot{M}_{\text{out}}^{\text{GRF}} \approx -5.7 M_{\odot} \text{ yr}^{-1}$, which is consistent with the estimate by Joung et al. (2012) for another simulated Milky-Way analog. The net flow rates of cold and hot gases are less significant, with $\dot{M}_{\text{cold}}^{\text{GRF}} \approx 0.05 M_{\odot} \text{ yr}^{-1}$ and $\dot{M}_{\text{hot}}^{\text{GRF}} \approx 0.15 M_{\odot} \text{ yr}^{-1}$. When switching the velocities from the GRF (hatched) to the LSR (solid), the changes in the net flow rates are subtle.

However, when examining gas inflows and outflows separately, we find that \dot{M}_{in} and \dot{M}_{out} are changed by a factor of ~ 10 for cold gas when velocities are corrected from the LSR to the GRF, while cool, warm, and hot gases are less affected. For example, the bottom panel shows that the inflow rate for cold CGM gas within 15 kpc is $\dot{M}_{\text{in}}^{\text{LSR}} \approx -0.25 M_{\odot} \text{ yr}^{-1}$ measured in the LSR, whereas the true accretion rate toward the galaxy center is $\dot{M}_{\text{in}}^{\text{GRF}} \approx -0.05 M_{\odot}$.

When applied to the Milky Way’s CGM studies, the bottom panel in Figure 10 suggests that \dot{M}_{in} calculated for H I HVCs in the Milky Way is likely to be overesti-

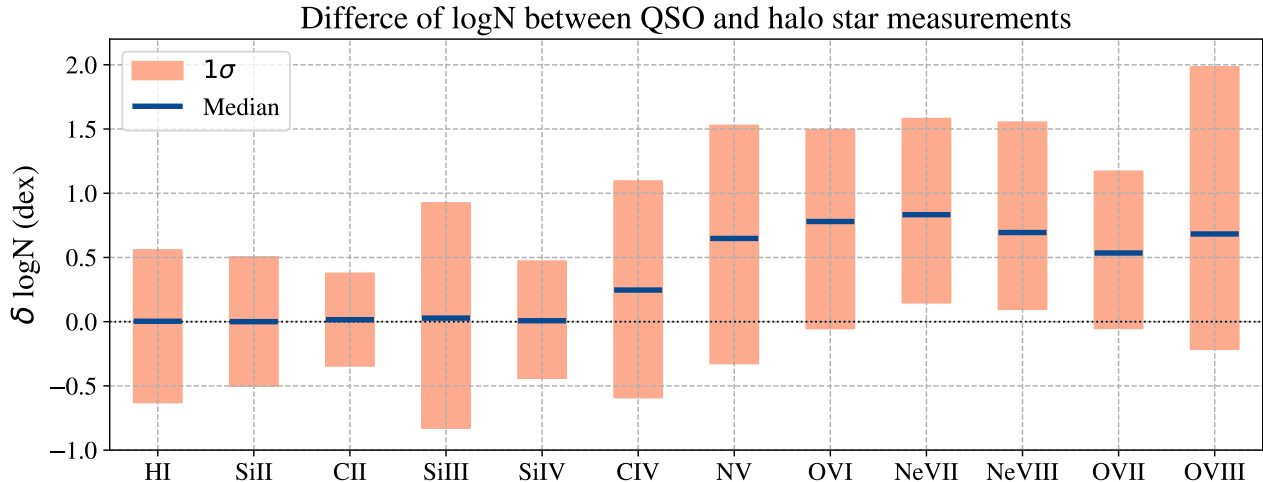


Figure 11. Differences of $\log N$ between random pairs of stellar and QSO sightlines for a list of ions, which are ordered according to their ionization potentials. Stars are placed at 5–15 kpc, and QSO are placed at R_{200} . Solid dark-blue line is for median value, and orange patches show 1σ (68%) confidence range. The large 1σ spread indicates the clumpiness of the simulated CGM in various phases. When applied to the Milky Way’s CGM, we find it more likely to detect the outer CGM in N v and O vi (in UV) or Ne vii, Ne viii, O vii, and O viii (in X-ray) through QSO-star pair studies.

mated if the cold gas is mostly at rest with the Galaxy’s rest frame. For example, Wakker et al. (2007) estimate an infall rate of $\dot{M}_{\text{in}} = -(0.1\text{--}0.25) M_{\odot} \text{ yr}^{-1}$ for the H I Complex C in LSR (e.g., Wakker et al. 2007), whereas Putman et al. (2012) suggest that the best-fit value of \dot{M}_{in} for all the major H I HVCs (including Complex C) is only $-0.08 M_{\odot} \text{ yr}^{-1}$ once they correct gas velocities from the LSR to the GRF with assumptions on gas tangential velocities and 3-dimensional spatial distribution (see their section 6.1). On the other hand, our result on cool and warm gases indicates that \dot{M}_{in} estimated for ionized HVCs in the Milky Way’s CGM are not significantly biased due to rest frame effects (e.g., Lehner & Howk 2011; Richter et al. 2017; Fox et al. 2019).

We note that, the adopted definition of \dot{M} does not reflect the actual infall rate because it assumes the gas in question would travel to the disk (D_i) at constant speed (v_i) without mass changes. In addition, it assumes that gas does not experience phase changes along its trajectory. Despite its broad use in observations, such a definition should be challenged because we have commonly seen in simulations that clouds may not travel far (\sim a few to ten kpc) without disruption due to interactions with ambient medium (Joung et al. 2012; Schneider et al. 2018; Gronke & Oh 2018, 2019; Banda-Barragán et al. 2019; Li et al. 2019). Therefore, the \dot{M} adopted here is also biased despite the correction of observing rest frames. To quantify this bias, one needs to monitor the evolution of gas phases across time, which is beyond the scope of this paper. We defer the analysis to another up-

coming FOGGIE project to address the bias inherited in \dot{M} calculation.

5.3. Observational Bias III: Stellar Sightlines v.s. QSO Sightlines

As noted in §1, an open issue in the Milky Way’s CGM studies is the ability of using QSO absorption lines to trace very low density gas in the outer CGM beyond ~ 15 kpc. Zheng et al. (2019a) show that Si iv column densities measured toward QSO sightlines cannot be fitted by a plane-parallel model that only accounts for nearby gas, and they propose an additional global component resembling the outer CGM to remedy the problem. Other efforts are underway to examine if the Milky Way’s outer CGM can be probed by comparing UV absorption line signatures of close pairs of halo stars and QSO sightlines (e.g., QuaStar; PI Peek). In such experiments, the halo stars provide measurements of ion column densities contributed by gas in the foreground of the stars, which will be subtracted off when compared with data from QSO sightlines at close angular separations. Here we construct a similar halo star-QSO experiment using synthetic observations on the simulated galaxy, and predict which ions are good tracers of the Milky Way’s outer CGM. The experiment is conducted with respect to the fiducial off-center observer, and we note that the location of the off-center observer does not matter significantly because we focus on gas distribution beyond 15 kpc and no kinematics are involved.

We first place mock stars in the simulated halos at distances of 5–15 kpc from the fiducial off-center ob-

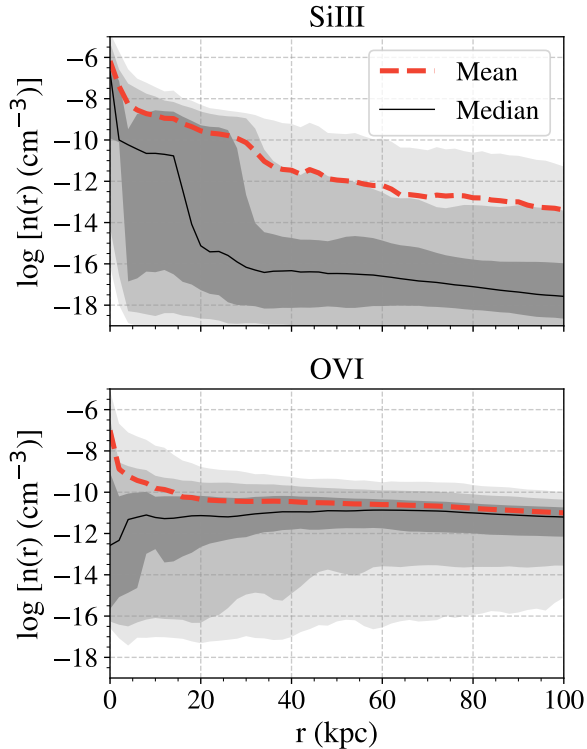


Figure 12. Si III radial density profile (top) and O VI radial density profile (bottom). The dark, median, and light contours show 1σ , 2σ , 3σ confidence range per radius bin. We find that Si III density quickly drops off beyond 30 kpc, while O VI’s remains relatively flat. The differences in radial profiles among various ions determine their detectability in QSO-star pair sightline studies. See § 5.3 and §5.4.

server to be consistent with current estimates on the distances of H I and ionized HVCs in the Milky Way (see §1; and e.g., Wakker 2004; Putman et al. 2012; Lehner et al. 2012). Ideally, we should place QSOs at higher redshifts to account for contamination from intervening absorbers. Since we focus on the difference in QSO-star sightlines due to existence of the Milky Way’s outer CGM sandwiched in between, here we simply the process by putting QSOs at the edge of the simulated CGM (R_{200}). All QSO and stellar sightlines are at $|b| > 20^\circ$ to mitigate contamination of nearby ISM. We generate 3×10^4 sightlines for both the star and QSO samples, and calculate the logarithmic column density differences ($\delta \log N = \log N_{\text{qso}} - \log N_{\text{star}}$) of any random pairs of QSO-star sightlines.

In Figure 11, we show median $\delta \log N$ values with 1σ range propagated through Monte Carlo method. A general impression is that $\delta \log N$ has a wide spread ($1\sigma \sim 0.3\text{--}1.0$ dex) regardless of the ion considered, suggesting that this simulated CGM is highly clumpy for its rich gaseous structures (see Figures 5 & 6). Among

all the ions, our result predicts that high ions, such as N V and O VI, are better UV tracers of the outer CGM beyond 15 kpc than low ions (i.e., Si II, C II, Si III, Si IV) for their positive $\delta \log N$ offsets. It is unclear whether C IV would be detectable in QSO-star pair sightline studies. On one hand, the positive mean offset of $\delta \log N \sim 0.25$ dex suggests that current spectroscopic instruments (e.g., HST/COS) should be able to identify the C IV absorption excess in QSO sightlines. On the other hand, the clumpiness of the halo gas may result in large $\log N$ scatters ($1\sigma \sim 0.8$ dex), which will dominate over the $\delta \log N$ excess.

We argue that the difference in $\delta \log N$ among various ions is rooted in their distinct radial density profiles. For example, as shown in Figure 12, Si III has a sharp decline in $n(r)$ values around 30 kpc, while O VI’s $n(r)$ profile remains relatively flat out to large radii. Therefore, QSO sightlines will collect more O VI from the outer CGM to result in detectable positive $\delta \log N$ offset in Figure 11. Generally speaking, high ions are distributed more broadly in the outer CGM, while low ions tend to be denser in the inner CGM.

Existing and ongoing studies offer multiple ways to test our prediction. For example, similar levels of $\delta \log N$ scatters are reported in star-star pair sightline studies for a range of ions, including O VI, Si IV, C IV, and Ca II (e.g., Howk et al. 2002; Bish et al. 2019; Werk et al. 2019). This implies that the clumpiness of the simulated CGM gas in FOGGIE is approaching what is measured from observations, although we note that in our exercise the statistics comes from random pairs of sightlines instead of pairs with close angular separation. On the other hand, Figure 11 suggests that Si IV in the Milky Way’s outer CGM may not be detectable, which is in stark contrast with Zheng et al. (2019a)’s result; there Zheng et al. (2019a) show that the Milky Way’s outer CGM is traceable in Si IV by analyzing 132 QSO absorption lines across the Galactic sky. The discrepancy between simulation and observation here suggests that the simulated galaxy may not be identical to the real Milky Way, and our prediction of the detectability of the Milky Way’s outer CGM in C IV, N V, and O VI remains to be tested.

5.4. Observational Bias IV:

Column Densities from Inside vs. External Views

Lastly, we tackle the conundrum that as the Milky Way residents, we always look at its CGM from the inside-out but observe other galaxies’ from external views. What is the observational bias when we compare the Milky Way’s data points to others? As Zheng et al. (2015) alluded to, the path lengths of the Milky Way’s

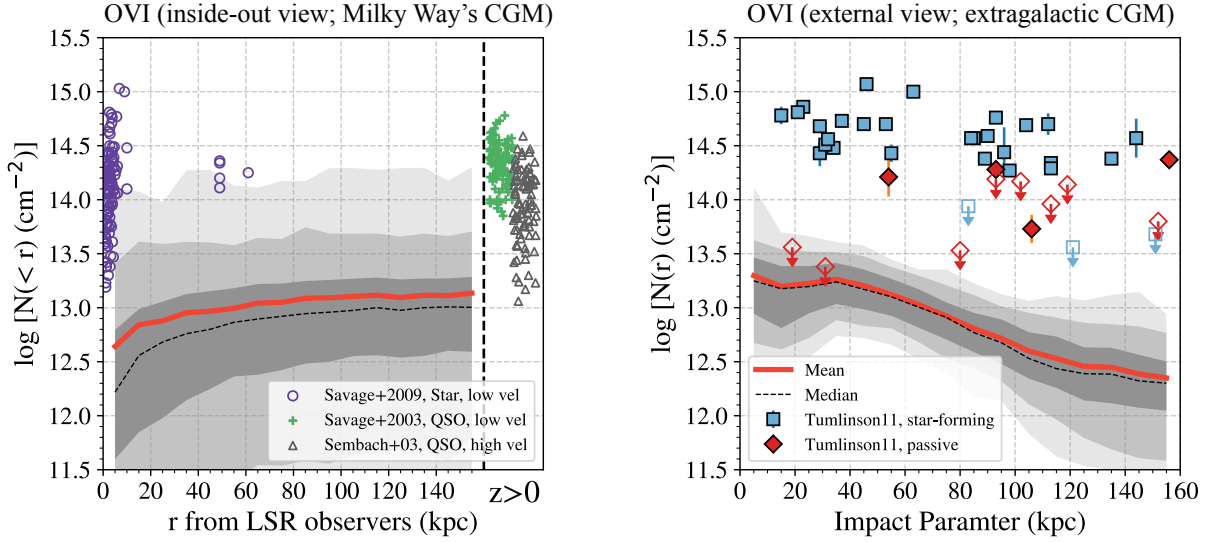


Figure 13. **Left:** $\log N_{\text{OVI}}(< r)$, cumulative O VI column density profile as seen from observers inside the galaxy. Red curve is the mean $\log N_{\text{OVI}}$ value within each r bin, and gray shades are 1σ , 2σ , and 3σ ranges, which are calculated by shooting 10^5 random sightlines through the simulated halo at $|b| \geq 20^\circ$. Open purple circles are low-velocity $\log N_{\text{OVI}}$ integrated over $-100 \lesssim v_{\text{LSR}} \lesssim 100 \text{ km s}^{-1}$ toward halo stars with known distances (Savage & Wakker 2009). Green crosses are low-velocity $\log N_{\text{OVI}}$ measured towards QSOs at $z > 0$ (Savage et al. 2003), and open gray triangles are high-velocity $\log N_{\text{OVI}}$ integrated over $v_{\text{LSR}} \lesssim -100 \text{ km s}^{-1}$ or $v_{\text{LSR}} \gtrsim +100 \text{ km s}^{-1}$ measured toward QSOs (Sembach et al. 2003). Typical $\log N_{\text{OVI}}$ errors for the Savage09, Savage03, and Sembach03 datasets are ~ 0.1 , 0.1 , 0.08 dex, respectively. **Right:** $\log N_{\text{OVI}}(r)$ profiles calculated with 10^5 random sightlines through the simulated halo from external views. Each sightline has a path length of $2R_{200}$. We overlay the $\log N_{\text{OVI}}(r)$ data from the COS-Halos survey (Tumlinson et al. 2011), with blue squares/red diamonds representing star-forming/passive galaxies. The figure shows that: (1) this simulation output under-produces $\log N_{\text{OVI}}$ as expected from observations, and (2) both observations and simulations show that $\log N$ measurements are subject to different observing angles and the distribution of gaseous structures in galaxy halos (e.g., radial inflows/outflows, cloud clumpiness). See §5.4 for more discussion.

CGM observations are only half of those in extragalactic systems, therefore, the column densities measured from inside-out views are a factor of two lower on average. They suggest that the Milky Way’s O VI column densities are consistent with extragalactic measurements (Tumlinson et al. 2011) if taking into account the discrepancy in path lengths.

Here we revisit their question but focus on the differences in column density profiles and scatters from inside-out and external views. In Figure 13, we show two example profiles using O VI and compare them with observations of the Milky Way’s CGM (Sembach et al. 2003; Savage et al. 2003; Savage & Wakker 2009) and extragalactic systems (Tumlinson et al. 2011). From both inside-out and external views, we find that the simulated halo does not produce sufficient O VI as the Milky Way and other $L \sim L_*$ galaxies. When there are data available, we find similar underproduction issues for other ions, such as H I, Si IV, C IV, N V, O VII (for the Milky Way observations, see Savage & Wakker 2009; Wakker et al. 2012; Fang et al. 2015; Zheng et al. 2019a; Prochaska & Zheng 2019; for extragalactic observations, see Werk et al. 2013; Bordoloi et al. 2014;

Liang & Chen 2014; Borthakur et al. 2015; Lehner et al. 2015; Prochaska et al. 2017; Keeney et al. 2017). Besides the reason for the H I under-production (§4), we suspect that the low ion column densities in this simulated halo are likely to be due to the thermal feedback recipe in FOGGIE (see discussion in §6). We note that similar $\log N_{\text{OVI}}$ under-production issues are found in other hydrodynamical simulations with various types of thermal feedback (e.g., Hummels et al. 2013; Ford et al. 2016; Liang et al. 2016; Gutcke et al. 2017; Suresh et al. 2017; Oppenheimer et al. 2018), while recent studies with non-thermal feedback implementation (e.g., cosmic rays, Salem et al. 2016; Butsky & Quinn 2018; Ji et al. 2019; Kempster & Quataert 2019) show promising solutions to boost $\log N_{\text{OVI}}$ production in CGM (see reviews by Somerville & Davé 2015; Tumlinson, Peeples, & Werk 2017).

Nevertheless, we find that the inside-out $\log N_{\text{OVI}}(< r)$ profile (left) shows larger $\log N$ scatter than the external profile (right), a phenomenon existing in both the synthetic and the real observational data. Specifically, observations of the Milky Way’s CGM show $\log N_{\text{OVI}}$ scatters up to ~ 1.5 dex, while extragalactic observa-

tions show $\lesssim 0.7$ dex fluctuation at fixed radii if we only consider the CGM detection in star-forming galaxies in COS-Halos. As we explain below, the different $\log N$ scatters between inside-out and external views are likely related to the structures and thermal status of ions in the CGM.

First, ion density profiles $n(r)$ and their density variances (or, halo clumpiness) determine that inside-out observing sightlines always have to pass through the inner CGM, which has higher density and is clumpier. For example, Figure 12 shows that the density scatter in the inner CGM ($r \lesssim 30$ kpc) is much higher than in the outer CGM. In other words, the denser and more clumpy gas in the inner CGM results in more $\log N$ variation from sightline to sightline. In contrast, external observations only pass through a small fraction of the inner CGM at close impact parameters, and most of the synthetic sightlines do not encounter large ion density variation beyond $r \gtrsim 30$ kpc.

Second, the radial pressure profiles we find in the simulated CGM (see Figures 5 & 6) determine that bulk motions (e.g., inflows, outflows) occur radially, and there is little motion along tangential directions. At a given radius, because gas is in thermal pressure equilibrium, hot gas is less dense than cold gas. Therefore, when observing such a CGM from the inside-out, one would find high $\log N$ scatters as their lines of sight move from low-density hot outflow regions to high-density cold inflow streams. Conversely, external observing sightlines only intercept these radial bulk motions tangentially. At a fixed impact parameter, $\log N$ values are averaged over a wide range of radial features, therefore, the corresponding $\log N$ scatter is reduced.

6. ADVANTAGES, CAVEATS, AND FUTURE DIRECTION

Our work highlights that studies of the Milky Way’s CGM have the advantage of directly measuring gas radial velocities; however, because the velocities are toward the Sun instead of the Milky Way center, observations of the Milky Way’s CGM are biased in various ways. We offer a promising solution to quantify and calibrate these biases through synthetic observations with a simulated Milky-Way analog. Many aspects of our work can be improved. Here we reflect upon the advantages and caveats in the FOGGIE/Mocky Way analyses, and discuss future directions for improvements.

The FOGGIE cosmological simulation (Peeples et al. 2019; Corlies et al. 2018) maps gaseous CGM structures at unprecedented spatial resolutions. Such zoom simulations have proven powerful in probing small scale structures and better resolving different phases and kinemat-

ics in CGM by many other authors with various codes and refinement schemes (van de Voort et al. 2019; Hummels et al. 2019; Suresh et al. 2019; Rhodin et al. 2019). First, the high, uniform resolution (0.19 kpc/ h comoving) in the CGM enables us to conduct synthetic observations such as QSO-star pair sightline comparison in §5.3, where resolution in the inner halo becomes critical in placing synthetic stellar sightlines. Second, the high spatial resolution better resolves the density structure in the CGM (Paper I), which is important for investigating column density scatter in the CGM from sightline to sightline, and from inside and external vies (see Figures 11 & 13). One could imagine the $\delta \log N$ scatter become unrealistic large with coarse simulation grids.

Caveats and challenges also emerge as we progress. The first challenge we encounter is to select a Milky-Way-like halo. By “Milky-Way-like”, we mean similar mass/phase quantities, rotation, and most importantly, similar gas features and distributions over the sky. The current generation of FOGGIE simulations focuses on six Milky-Way-mass halos, which are described in detail in Paper IV (R. Simons et al., in preparation). The simulation output we analyze in this work is one of the least massive ones among all FOGGIE-selected halos. Despite its similar disk size (r_s, z_s), the simulation produces far less H I and other ions in its CGM than the Milky Way (e.g., Figures 3, 7, 13). As we point out in §3.1 and 4, the gravitational potential is not well resolved along the z direction, likely resulting in an incorrect distribution of H I across the sky. Therefore, in future work, one should aim to increase the disk resolution to better simulate the structure of the ISM (e.g. Christensen et al. 2010). In addition, as we show in §5.4, FOGGIE’s thermal feedback is unable to produce expel as many metals into the CGM and thus reproduce the high ionic column densities as observed in the Milky Way and extragalactic CGM (see also Hamilton-Campos et al. 2020). Non-thermal feedback, such as radiation pressure from hot stars (Hopkins et al. 2014) and non-thermal pressure support, such as magnetic fields and cosmic rays, is likely to be critical to alleviate these issues.

The second caveat in our work is that our synthetic observations do not consider how physical quantities translate into observables through the lens of instruments. Here we study gas distribution and flux rates by directly integrating the corresponding quantities in velocity and position space. Ideally, synthetic spectroscopy (e.g., as in Paper I) would be of great use to assess how physical information could be missed because of systemic instrument effects. Our ultimate goal is to conduct synthetic spectroscopy to generate ion absorption lines and take into account observational limitation, such as in-

struments' point spread function, signal-to-noise ratio, Voigt-profile fitting, and sightline selection effect.

7. SUMMARY OF MOCKY WAY

Observations of the Milky Way's CGM are highly biased because we reside inside the Galaxy at an off-center location. Gas in the Milky Way's CGM, especially at low velocities, is mostly obscured by nearby dense ISM material. In addition, gas velocities measured along lines of sight toward the Sun do not represent true velocity values in the Galactic rest frame, which affects estimates of gas inflow and outflow rates in the Milky Way. In this work we investigate four observational biases inherent in the Milky Way's CGM studies with mock observations of a Milky-Way analog from FOGGIE.

We first examine the physical properties of the simulated galaxy and find that they are largely consistent with the Milky Way values on the same order of magnitude (see Table 1 and §3). The CGM exhibits rich kinematic structures as we show in Figures 5 and 6 (see §3.2). We find bipolar outflows at high velocities ($v \gtrsim 100 \text{ km s}^{-1}$), high temperature ($T \gtrsim 10^6 \text{ K}$), and high metallicities (~ 0.1 to $> 1Z_{\odot}$). By contrast, large-scale filamentary inflows bypass the outflows; they are observed to be moving at $v \lesssim -100 \text{ km s}^{-1}$, with low temperature ($T \lesssim 10^5 \text{ K}$) and low metallicity ($Z \lesssim 0.01 Z_{\odot}$). These filamentary inflows are not directly accreted onto the central galaxy. Instead, they mix with ambient medium in the inner CGM at $r \lesssim 20 \text{ kpc}$. Gas at low velocities, both inflows and outflows, fill most of the volume of the CGM, and exist co-spatially. Overall, the cool and warm CGM gases are dominantly infalling toward the center of the galaxy, with a total net infall rate of $-5.7 M_{\odot} \text{ yr}^{-1}$ (Figure 10).

We build a mock galactic coordinate system similar to that of the Milky Way (§4). The mock observer is placed at twice the disk scale length ($d_{\text{obs}} = 2r_s$) to be consistent with the location of the Sun in the Milky Way. In §5, we investigate four observational biases pertaining to the Milky Way's CGM studies by comparing the observable quantities with those directly estimated for the simulated CGM. We summarize here the four biases.

Bias I: in §5.1, we revisit the question put forward by Zheng et al. (2015) and estimate the fraction of CGM mass being missed in high-velocity-focused studies of the Milky Way's CGM. We find that $\sim 2/3$ of the total CGM mass is moving at low velocities ($|v_{\text{LSR}}| < 100 \text{ km s}^{-1}$), thus eluding detection. When broken down into different phases, we find a similar mass fraction of cold, cool, warm, and hot gas moving at low velocities, thus missing from observations (Figure 9).

Bias II: in §5.2, we discuss how current estimates on mass inflow rates (\dot{M}_{in}) of the Milky Way's CGM could be biased because gas velocities are measured along observers' lines of sight (i.e., v_{LSR} or v_{GSR}) instead of toward the galaxy center (v_{GRF}). We find that, the \dot{M}_{in} value for cold CGM gas within 15 kpc is reduced by a factor of ~ 5 (from $-0.25 M_{\odot} \text{ yr}^{-1}$ to $-0.05 M_{\odot} \text{ yr}^{-1}$) when we correct the gas velocities from the LSR to the GRF (Figure 10), while the \dot{M}_{in} values for cool, warm, and hot gases do not change significantly when switching the rest frames. Our result suggests that the H I HVCs infall rates in the Milky Way maybe overestimated if the rest frame biases are not taken into account.

Bias III: in §5.3, we investigate whether QSO absorption lines are sensitive to probe the Milky Way's outer CGM ($r \gtrsim 15 \text{ kpc}$) and what ions are good tracers. We generate halo star sightlines randomly distributed between 5 to 15 kpc to collect gas column densities for a range of ions (H I, Si II, Si III, Si IV, C II, C IV, N V, O VI, O VII, O VIII, Ne VII, Ne VIII). Similarly, we generate random QSO sightlines through the entire halo (out to R_{200}). Through comparison of random QSO-star pair sightlines, we find that O VI and N V are likely to be good UV tracers of the Milky Way's outer CGM for their large, detectable column density difference ($\delta \log N \gtrsim 0.6$ dex) between QSO and star measurements. C IV may be less sensitive because the $\delta \log N$ difference between QSO and stars is likely to be overwhelmed by the column density scatter from sightline to sightline.

Bias IV: in §5.4, we study how observations of the Milky Way's CGM (inside-out views) could differ from extragalactic observations (external views). Both observations and the simulation show that the $\log N$ scatter from inside-out views is a factor of ~ 2 higher than those from external views. The discrepancy is because observing sightlines from inside-out views always have to pass through the inner halo gases which are denser and more clumpy. And, because gas inflows and outflows are distributed radially (Figures 5, 6), observations with inside-out views encounter more variances from sightline to sightline depending on whether or not the lines of sight are along inflowing or outflowing features.

We thank M. Putman, A. Fox, and N. Lehner for their helpful discussion and feedback in improving this manuscript. Y.Z. acknowledges support from the Miller Institute for Basic Research in Science at the University of California, Berkeley. B.W.O. was supported in part by NSF grants PHY-1430152, AST-1514700, and OAC-1835213, by NASA grants NNX12AC98G and NNX15AP39G, and by HST AR #14315. Resources supporting this work were provided by the NASA High-

End Computing (HEC) Program through the NASA Advanced Supercomputing (NAS) Division at Ames Research Center and were sponsored by NASA’s Science Mission Directorate; we are grateful for the superb user-support provided by NAS. Resources were also provided by the Blue Waters sustained-petascale computing project, which is supported by the NSF (award number ACI 1238993 and ACI-1514580) and the state of Illinois. Blue Waters is a joint effort of the University of Illinois at Urbana-Champaign and its NCSA. This work benefited from the milky-way and haha emojis on Slack. We have made extensive use of the python libraries Astropy, a community-developed core Python package for Astronomy (The Astropy Collaboration et al.

2018, <http://www.astropy.org>) and seaborn. Computations described in this work were performed using the publicly-available Enzo code, which is the product of a collaborative effort of many independent scientists from numerous institutions around the world.

Facilities: NASA Pleiades, NCSA Blue Waters

Software: astropy (The Astropy Collaboration et al. 2018), Cloudy (Ferland et al. 2013), Enzo (Bryan et al. 2014), grackle (Smith et al. 2017), yt (Turk et al. 2011), Trident (Hummels, Smith, & Silvia 2017)

REFERENCES

- Auld, R., Minchin, R. F., Davies, J. I., et al. 2006, MNRAS, 371, 1617, doi: [10.1111/j.1365-2966.2006.10761.x](https://doi.org/10.1111/j.1365-2966.2006.10761.x)
- Bahcall, J. N., & Spitzer, Lyman, J. 1969, ApJL, 156, L63, doi: [10.1086/180350](https://doi.org/10.1086/180350)
- Banda-Barragán, W. E., Zertuche, F. J., Federrath, C., et al. 2019, MNRAS, 486, 4526, doi: [10.1093/mnras/stz1040](https://doi.org/10.1093/mnras/stz1040)
- Berg, M. A., Howk, J. C., Lehner, N., et al. 2019, ApJ, 883, 5, doi: [10.3847/1538-4357/ab378e](https://doi.org/10.3847/1538-4357/ab378e)
- Berg, T. A. M., Ellison, S. L., Tumlinson, J., et al. 2018, MNRAS, 478, 3890, doi: [10.1093/mnras/sty962](https://doi.org/10.1093/mnras/sty962)
- Bish, H. V., Werk, J. K., Prochaska, J. X., et al. 2019, ApJ, 882, 76, doi: [10.3847/1538-4357/ab3414](https://doi.org/10.3847/1538-4357/ab3414)
- Bland, J., & Tully, B. 1988, Nature, 334, 43, doi: [10.1038/334043a0](https://doi.org/10.1038/334043a0)
- Bland-Hawthorn, J., & Gerhard, O. 2016, ARA&A, 54, 529, doi: [10.1146/annurev-astro-081915-023441](https://doi.org/10.1146/annurev-astro-081915-023441)
- Bordoloi, R., Lilly, S. J., Knobel, C., et al. 2011, ApJ, 743, 10, doi: [10.1088/0004-637X/743/1/10](https://doi.org/10.1088/0004-637X/743/1/10)
- Bordoloi, R., Tumlinson, J., Werk, J. K., et al. 2014, ApJ, 796, 136, doi: [10.1088/0004-637X/796/2/136](https://doi.org/10.1088/0004-637X/796/2/136)
- Bordoloi, R., Fox, A. J., Lockman, F. J., et al. 2017, ApJ, 834, 191, doi: [10.3847/1538-4357/834/2/191](https://doi.org/10.3847/1538-4357/834/2/191)
- Borthakur, S., Heckman, T., Tumlinson, J., et al. 2015, ApJ, 813, 46, doi: [10.1088/0004-637X/813/1/46](https://doi.org/10.1088/0004-637X/813/1/46)
- Bregman, J. N., Anderson, M. E., Miller, M. J., et al. 2018, ApJ, 862, 3, doi: [10.3847/1538-4357/aacafe](https://doi.org/10.3847/1538-4357/aacafe)
- Brummel-Smith, C., Bryan, G., Butsky, I., et al. 2019, The Journal of Open Source Software, 4, 1636, doi: [10.21105/joss.01636](https://doi.org/10.21105/joss.01636)
- Bryan, G. L., Norman, M. L., O’Shea, B. W., et al. 2014, ApJS, 211, 19, doi: [10.1088/0067-0049/211/2/19](https://doi.org/10.1088/0067-0049/211/2/19)
- Burchett, J. N., Tripp, T. M., Bordoloi, R., et al. 2016, ApJ, 832, 124, doi: [10.3847/0004-637X/832/2/124](https://doi.org/10.3847/0004-637X/832/2/124)
- Burchett, J. N., Tripp, T. M., Prochaska, J. X., et al. 2019, ApJL, 877, L20, doi: [10.3847/2041-8213/ab1f7f](https://doi.org/10.3847/2041-8213/ab1f7f)
- Butsky, I., & Quinn, T. R. 2018, ArXiv e-prints. <https://arxiv.org/abs/1803.06345>
- Chen, H.-W., Helsby, J. E., Gauthier, J.-R., et al. 2010, ApJ, 714, 1521, doi: [10.1088/0004-637X/714/2/1521](https://doi.org/10.1088/0004-637X/714/2/1521)
- Chen, H.-W., & Mulchaey, J. S. 2009, ApJ, 701, 1219, doi: [10.1088/0004-637X/701/2/1219](https://doi.org/10.1088/0004-637X/701/2/1219)
- Chen, H.-W., Zahedy, F. S., Johnson, S. D., et al. 2018, MNRAS, 479, 2547, doi: [10.1093/mnras/sty1541](https://doi.org/10.1093/mnras/sty1541)
- Christensen, C. R., Quinn, T., Stinson, G., Bellovary, J., & Wadsley, J. 2010, ApJ, 717, 121, doi: [10.1088/0004-637X/717/1/121](https://doi.org/10.1088/0004-637X/717/1/121)
- Clark, S. E., Peek, J. E. G., & Putman, M. E. 2014, ApJ, 789, 82, doi: [10.1088/0004-637X/789/1/82](https://doi.org/10.1088/0004-637X/789/1/82)
- Corlies, L., Peeples, M. S., Tumlinson, J., et al. 2018, ArXiv e-prints. <https://arxiv.org/abs/1811.05060>
- Dickey, J. M., & Lockman, F. J. 1990, ARA&A, 28, 215, doi: [10.1146/annurev.aa.28.090190.001243](https://doi.org/10.1146/annurev.aa.28.090190.001243)
- Diplas, A., & Savage, B. D. 1991, ApJ, 377, 126, doi: [10.1086/170341](https://doi.org/10.1086/170341)
- El-Badry, K., Quataert, E., Wetzel, A., et al. 2018, MNRAS, 473, 1930, doi: [10.1093/mnras/stx2482](https://doi.org/10.1093/mnras/stx2482)
- Emerick, A., Bryan, G. L., & Mac Low, M.-M. 2018, ApJL, 865, L22, doi: [10.3847/2041-8213/aae315](https://doi.org/10.3847/2041-8213/aae315)
- Fang, T., Buote, D., Bullock, J., & Ma, R. 2015, ApJS, 217, 21, doi: [10.1088/0067-0049/217/2/21](https://doi.org/10.1088/0067-0049/217/2/21)
- Ferland, G. J., Porter, R. L., van Hoof, P. A. M., et al. 2013, RMxAA, 49, 137. <https://arxiv.org/abs/1302.4485>
- Fernández, X., Gim, H. B., van Gorkom, J. H., et al. 2016, ApJL, 824, L1, doi: [10.3847/2041-8205/824/1/L1](https://doi.org/10.3847/2041-8205/824/1/L1)
- Fielding, D., Quataert, E., McCourt, M., & Thompson, T. A. 2017, MNRAS, 466, 3810, doi: [10.1093/mnras/stw3326](https://doi.org/10.1093/mnras/stw3326)

- Ford, A. B., Davé, R., Oppenheimer, B. D., et al. 2014, MNRAS, 444, 1260, doi: [10.1093/mnras/stu1418](https://doi.org/10.1093/mnras/stu1418)
- Ford, A. B., Werk, J. K., Davé, R., et al. 2016, MNRAS, 459, 1745, doi: [10.1093/mnras/stw595](https://doi.org/10.1093/mnras/stw595)
- Fox, A. J., Richter, P., Ashley, T., et al. 2019, ApJ, 884, 53, doi: [10.3847/1538-4357/ab40ad](https://doi.org/10.3847/1538-4357/ab40ad)
- Fox, A. J., Wakker, B. P., Barger, K. A., et al. 2014, ApJ, 787, 147, doi: [10.1088/0004-637X/787/2/147](https://doi.org/10.1088/0004-637X/787/2/147)
- Gibbons, S. L. J., Belokurov, V., & Evans, N. W. 2014, MNRAS, 445, 3788, doi: [10.1093/mnras/stu1986](https://doi.org/10.1093/mnras/stu1986)
- Gronke, M., & Oh, S. P. 2018, MNRAS, 480, L111, doi: [10.1093/mnrasl/sly131](https://doi.org/10.1093/mnrasl/sly131)
- . 2019, MNRAS, 2995, doi: [10.1093/mnras/stz3332](https://doi.org/10.1093/mnras/stz3332)
- Gutcke, T. A., Stinson, G. S., Macciò, A. V., Wang, L., & Dutton, A. A. 2017, MNRAS, 464, 2796, doi: [10.1093/mnras/stw2539](https://doi.org/10.1093/mnras/stw2539)
- Hamilton-Campos, K. A., Simons, R., Peeples, M., & Tumlinson, J. 2020, in American Astronomical Society Meeting Abstracts, Vol. 52, American Astronomical Society Meeting Abstracts, 207.07
- Heckman, T., Borthakur, S., Wild, V., Schiminovich, D., & Bordoloi, R. 2017, ApJ, 846, 151, doi: [10.3847/1538-4357/aa80dc](https://doi.org/10.3847/1538-4357/aa80dc)
- HI4PI Collaboration, Ben Bekhti, N., Flöer, L., et al. 2016, A&A, 594, A116, doi: [10.1051/0004-6361/201629178](https://doi.org/10.1051/0004-6361/201629178)
- Ho, S. H., Martin, C. L., Kacprzak, G. G., & Churchill, C. W. 2017, ApJ, 835, 267, doi: [10.3847/1538-4357/835/2/267](https://doi.org/10.3847/1538-4357/835/2/267)
- Hopkins, P. F., Kereš, D., Oñorbe, J., et al. 2014, MNRAS, 445, 581, doi: [10.1093/mnras/stu1738](https://doi.org/10.1093/mnras/stu1738)
- Howk, J. C., Savage, B. D., Sembach, K. R., & Hoopes, C. G. 2002, ApJ, 572, 264, doi: [10.1086/340231](https://doi.org/10.1086/340231)
- Hummels, C. B., Bryan, G. L., Smith, B. D., & Turk, M. J. 2013, MNRAS, 430, 1548, doi: [10.1093/mnras/sts702](https://doi.org/10.1093/mnras/sts702)
- Hummels, C. B., Smith, B. D., & Silvia, D. W. 2017, ApJ, 847, 59, doi: [10.3847/1538-4357/aa7e2d](https://doi.org/10.3847/1538-4357/aa7e2d)
- Hummels, C. B., Smith, B. D., Hopkins, P. F., et al. 2019, ApJ, 882, 156, doi: [10.3847/1538-4357/ab378f](https://doi.org/10.3847/1538-4357/ab378f)
- Ji, S., Chan, T. K., Hummels, C. B., et al. 2019, arXiv e-prints, arXiv:1909.00003. <https://arxiv.org/abs/1909.00003>
- Johnson, S. D., Chen, H.-W., & Mulchaey, J. S. 2015, MNRAS, 452, 2553, doi: [10.1093/mnras/stv1481](https://doi.org/10.1093/mnras/stv1481)
- Johnson, S. D., Chen, H.-W., Mulchaey, J. S., Schaye, J., & Straka, L. A. 2017, ApJL, 850, L10, doi: [10.3847/2041-8213/aa9370](https://doi.org/10.3847/2041-8213/aa9370)
- Joung, M. R., Putman, M. E., Bryan, G. L., Fernández, X., & Peek, J. E. G. 2012, ApJ, 759, 137, doi: [10.1088/0004-637X/759/2/137](https://doi.org/10.1088/0004-637X/759/2/137)
- Kacprzak, G. G., Churchill, C. W., & Nielsen, N. M. 2012, ApJL, 760, L7, doi: [10.1088/2041-8205/760/1/L7](https://doi.org/10.1088/2041-8205/760/1/L7)
- Kafle, P. R., Sharma, S., Lewis, G. F., & Bland-Hawthorn, J. 2012, ApJ, 761, 98, doi: [10.1088/0004-637X/761/2/98](https://doi.org/10.1088/0004-637X/761/2/98)
- Kalberla, P. M. W., Burton, W. B., Hartmann, D., et al. 2005, A&A, 440, 775, doi: [10.1051/0004-6361:20041864](https://doi.org/10.1051/0004-6361:20041864)
- Kalberla, P. M. W., & Dedes, L. 2008, A&A, 487, 951, doi: [10.1051/0004-6361:20079240](https://doi.org/10.1051/0004-6361:20079240)
- Kalberla, P. M. W., Dedes, L., Kerp, J., & Haud, U. 2007, A&A, 469, 511, doi: [10.1051/0004-6361:20066362](https://doi.org/10.1051/0004-6361:20066362)
- Keeney, B. A., Stocke, J. T., Danforth, C. W., et al. 2017, ApJS, 230, 6, doi: [10.3847/1538-4365/aa6b59](https://doi.org/10.3847/1538-4365/aa6b59)
- Kempski, P., & Quataert, E. 2019, arXiv e-prints, arXiv:1908.10367. <https://arxiv.org/abs/1908.10367>
- Koposov, S. E., Rix, H.-W., & Hogg, D. W. 2010, ApJ, 712, 260, doi: [10.1088/0004-637X/712/1/260](https://doi.org/10.1088/0004-637X/712/1/260)
- Küpper, A. H. W., Balbinot, E., Bonaca, A., et al. 2015, ApJ, 803, 80, doi: [10.1088/0004-637X/803/2/80](https://doi.org/10.1088/0004-637X/803/2/80)
- Lan, T.-W., & Mo, H. 2018, ApJ, 866, 36, doi: [10.3847/1538-4357/aadc08](https://doi.org/10.3847/1538-4357/aadc08)
- Lau, M. W., Prochaska, J. X., & Hennawi, J. F. 2018, ApJ, 857, 126, doi: [10.3847/1538-4357/aab78e](https://doi.org/10.3847/1538-4357/aab78e)
- Lehner, N., & Howk, J. C. 2011, Science, 334, 955, doi: [10.1126/science.1209069](https://doi.org/10.1126/science.1209069)
- Lehner, N., Howk, J. C., Thom, C., et al. 2012, MNRAS, 424, 2896, doi: [10.1111/j.1365-2966.2012.21428.x](https://doi.org/10.1111/j.1365-2966.2012.21428.x)
- Lehner, N., Howk, J. C., & Wakker, B. P. 2015, ApJ, 804, 79, doi: [10.1088/0004-637X/804/2/79](https://doi.org/10.1088/0004-637X/804/2/79)
- . 2017, ApJ, 848, 71, doi: [10.3847/1538-4357/aa8e4a](https://doi.org/10.3847/1538-4357/aa8e4a)
- Levine, E. S., Blitz, L., & Heiles, C. 2006, ApJ, 643, 881, doi: [10.1086/503091](https://doi.org/10.1086/503091)
- Li, M., Bryan, G. L., & Ostriker, J. P. 2017, ApJ, 841, 101, doi: [10.3847/1538-4357/aa7263](https://doi.org/10.3847/1538-4357/aa7263)
- Li, Y., & Bryan, G. L. 2014, ApJ, 789, 153, doi: [10.1088/0004-637X/789/2/153](https://doi.org/10.1088/0004-637X/789/2/153)
- Li, Z., Hopkins, P. F., Squire, J., & Hummels, C. 2019, MNRAS, 3180, doi: [10.1093/mnras/stz3567](https://doi.org/10.1093/mnras/stz3567)
- Liang, C. J., & Chen, H.-W. 2014, MNRAS, 445, 2061, doi: [10.1093/mnras/stu1901](https://doi.org/10.1093/mnras/stu1901)
- Liang, C. J., Kravtsov, A. V., & Agertz, O. 2016, MNRAS, 458, 1164, doi: [10.1093/mnras/stw375](https://doi.org/10.1093/mnras/stw375)
- Lochhaas, C., Bryan, G. L., Li, Y., Li, M., & Fielding, D. 2019, arXiv e-prints, arXiv:1908.00021. <https://arxiv.org/abs/1908.00021>
- Lopez, S., Tejos, N., Ledoux, C., et al. 2018, Nature, 554, 493, doi: [10.1038/nature25436](https://doi.org/10.1038/nature25436)
- López-Corredoira, M. 2014, A&A, 563, A128, doi: [10.1051/0004-6361/201423505](https://doi.org/10.1051/0004-6361/201423505)
- Lozinskaya, T. A., & Kardashev, N. S. 1963, Soviet Ast., 7, 161

- Martin, C. L., Ho, S. H., Kacprzak, G. G., & Churchill, C. W. 2019, *ApJ*, 878, 84, doi: [10.3847/1538-4357/ab18ac](https://doi.org/10.3847/1538-4357/ab18ac)
- Münch, G., & Zirin, H. 1961, *ApJ*, 133, 11, doi: [10.1086/146999](https://doi.org/10.1086/146999)
- Nelson, D., Pillepich, A., Springel, V., et al. 2019, *MNRAS*, 490, 3234, doi: [10.1093/mnras/stz2306](https://doi.org/10.1093/mnras/stz2306)
- Nidever, D. L., Majewski, S. R., & Butler Burton, W. 2008, *ApJ*, 679, 432, doi: [10.1086/587042](https://doi.org/10.1086/587042)
- Nielsen, N. M., Churchill, C. W., Kacprzak, G. G., Murphy, M. T., & Evans, J. L. 2016, *ApJ*, 818, 171, doi: [10.3847/0004-637X/818/2/171](https://doi.org/10.3847/0004-637X/818/2/171)
- Oppenheimer, B. D., Schaye, J., Crain, R. A., Werk, J. K., & Richings, A. J. 2018, *MNRAS*, 481, 835, doi: [10.1093/mnras/sty2281](https://doi.org/10.1093/mnras/sty2281)
- Peek, J. 2018, QuaStar: The first unobscured view of the Milky Way's Circumgalactic Medium, HST Proposal
- Peek, J. E. G., Babler, B. L., Zheng, Y., et al. 2018, *ApJS*, 234, 2, doi: [10.3847/1538-4365/aa91d3](https://doi.org/10.3847/1538-4365/aa91d3)
- Peeples, M. S., Corlies, L., Tumlinson, J., et al. 2019, *ApJ*, 873, 129, doi: [10.3847/1538-4357/ab0654](https://doi.org/10.3847/1538-4357/ab0654)
- Planck Collaboration, Ade, P. A. R., Aghanim, N., et al. 2014, *A&A*, 571, A16, doi: [10.1051/0004-6361/201321591](https://doi.org/10.1051/0004-6361/201321591)
- . 2016, *A&A*, 594, A13, doi: [10.1051/0004-6361/201525830](https://doi.org/10.1051/0004-6361/201525830)
- Prochaska, J. X., Weiner, B., Chen, H.-W., Cooksey, K. L., & Mulchaey, J. S. 2011, *ApJS*, 193, 28, doi: [10.1088/0067-0049/193/2/28](https://doi.org/10.1088/0067-0049/193/2/28)
- Prochaska, J. X., & Zheng, Y. 2019, *MNRAS*, 485, 648, doi: [10.1093/mnras/stz261](https://doi.org/10.1093/mnras/stz261)
- Prochaska, J. X., Werk, J. K., Worseck, G., et al. 2017, *ApJ*, 837, 169, doi: [10.3847/1538-4357/aa6007](https://doi.org/10.3847/1538-4357/aa6007)
- Putman, M. E., Peek, J. E. G., & Jounge, M. R. 2012, *ARA&A*, 50, 491, doi: [10.1146/annurev-astro-081811-125612](https://doi.org/10.1146/annurev-astro-081811-125612)
- Putman, M. E., de Heij, V., Staveley-Smith, L., et al. 2002, *AJ*, 123, 873, doi: [10.1086/338088](https://doi.org/10.1086/338088)
- Qu, Z., & Bregman, J. N. 2019, *ApJ*, 880, 89, doi: [10.3847/1538-4357/ab2a0b](https://doi.org/10.3847/1538-4357/ab2a0b)
- Reid, M. J., Menten, K. M., Brunthaler, A., et al. 2014, *ApJ*, 783, 130, doi: [10.1088/0004-637X/783/2/130](https://doi.org/10.1088/0004-637X/783/2/130)
- Rhodin, N. H. P., Agertz, O., Christensen, L., Renaud, F., & Fynbo, J. P. U. 2019, *MNRAS*, 488, 3634, doi: [10.1093/mnras/stz1479](https://doi.org/10.1093/mnras/stz1479)
- Richter, P., Fox, A. J., Wakker, B. P., et al. 2013, *ApJ*, 772, 111, doi: [10.1088/0004-637X/772/2/111](https://doi.org/10.1088/0004-637X/772/2/111)
- Richter, P., Nuza, S. E., Fox, A. J., et al. 2017, *A&A*, 607, A48, doi: [10.1051/0004-6361/201630081](https://doi.org/10.1051/0004-6361/201630081)
- Rubin, K. H. R., Diamond-Stanic, A. M., Coil, A. L., & Crighton, N. H. M. 2018, *ArXiv e-prints*, <https://arxiv.org/abs/1806.08801>
- Rubin, K. H. R., Prochaska, J. X., Koo, D. C., et al. 2014, *ApJ*, 794, 156, doi: [10.1088/0004-637X/794/2/156](https://doi.org/10.1088/0004-637X/794/2/156)
- Salem, M., Bryan, G. L., & Corlies, L. 2016, *MNRAS*, 456, 582, doi: [10.1093/mnras/stv2641](https://doi.org/10.1093/mnras/stv2641)
- Saul, D. R., Peek, J. E. G., Grcevich, J., et al. 2012, *ApJ*, 758, 44, doi: [10.1088/0004-637X/758/1/44](https://doi.org/10.1088/0004-637X/758/1/44)
- Savage, B. D., & Wakker, B. P. 2009, *ApJ*, 702, 1472, doi: [10.1088/0004-637X/702/2/1472](https://doi.org/10.1088/0004-637X/702/2/1472)
- Savage, B. D., Sembach, K. R., Wakker, B. P., et al. 2003, *ApJS*, 146, 125, doi: [10.1086/346229](https://doi.org/10.1086/346229)
- Schneider, E. E., Robertson, B. E., & Thompson, T. A. 2018, *ApJ*, 862, 56, doi: [10.3847/1538-4357/aacce1](https://doi.org/10.3847/1538-4357/aacce1)
- Schwarz, U. J., Wakker, B. P., & van Woerden, H. 1995, *A&A*, 302, 364
- Sembach, K. R., Wakker, B. P., Savage, B. D., et al. 2003, *ApJS*, 146, 165, doi: [10.1086/346231](https://doi.org/10.1086/346231)
- Shull, J. M., Jones, J. R., Danforth, C. W., & Collins, J. A. 2009, *ApJ*, 699, 754, doi: [10.1088/0004-637X/699/1/754](https://doi.org/10.1088/0004-637X/699/1/754)
- Smailagić, M., Prochaska, J. X., Burchett, J., Zhu, G., & Ménard, B. 2018, *ApJ*, 867, 106, doi: [10.3847/1538-4357/aae384](https://doi.org/10.3847/1538-4357/aae384)
- Smith, B. D., Bryan, G. L., Glover, S. C. O., et al. 2017, *MNRAS*, 466, 2217, doi: [10.1093/mnras/stw3291](https://doi.org/10.1093/mnras/stw3291)
- Sofue, Y., Honma, M., & Omodaka, T. 2009, *PASJ*, 61, 227, doi: [10.1093/pasj/61.2.227](https://doi.org/10.1093/pasj/61.2.227)
- Somerville, R. S., & Davé, R. 2015, *ARA&A*, 53, 51, doi: [10.1146/annurev-astro-082812-140951](https://doi.org/10.1146/annurev-astro-082812-140951)
- Spitzer, Lyman, J. 1956, *ApJ*, 124, 20, doi: [10.1086/146200](https://doi.org/10.1086/146200)
- Stanimirović, S., Hoffman, S., Heiles, C., et al. 2008, *ApJ*, 680, 276, doi: [10.1086/587480](https://doi.org/10.1086/587480)
- Stocke, J. T., Keeney, B. A., Danforth, C. W., et al. 2013, *ApJ*, 763, 148, doi: [10.1088/0004-637X/763/2/148](https://doi.org/10.1088/0004-637X/763/2/148)
- Suresh, J., Nelson, D., Genel, S., Rubin, K. H. R., & Hernquist, L. 2019, *MNRAS*, 483, 4040, doi: [10.1093/mnras/sty3402](https://doi.org/10.1093/mnras/sty3402)
- Suresh, J., Rubin, K. H. R., Kannan, R., et al. 2017, *MNRAS*, 465, 2966, doi: [10.1093/mnras/stw2499](https://doi.org/10.1093/mnras/stw2499)
- The Astropy Collaboration, Price-Whelan, A. M., Sipőcz, B. M., et al. 2018, *ArXiv e-prints*, <https://arxiv.org/abs/1801.02634>
- Thom, C., Peek, J. E. G., Putman, M. E., et al. 2008, *ApJ*, 684, 364, doi: [10.1086/589960](https://doi.org/10.1086/589960)
- Thompson, T. A., Quataert, E., Zhang, D., & Weinberg, D. H. 2016, *MNRAS*, 455, 1830, doi: [10.1093/mnras/stv2428](https://doi.org/10.1093/mnras/stv2428)
- Tumlinson, J., Peeples, M. S., & Werk, J. K. 2017, *ARA&A*, 55, 389, doi: [10.1146/annurev-astro-091916-055240](https://doi.org/10.1146/annurev-astro-091916-055240)
- Tumlinson, J., Thom, C., Werk, J. K., et al. 2011, *Science*, 334, 948, doi: [10.1126/science.1209840](https://doi.org/10.1126/science.1209840)

- . 2013, *ApJ*, 777, 59, doi: [10.1088/0004-637X/777/1/59](https://doi.org/10.1088/0004-637X/777/1/59)
- Turk, M. J., Smith, B. D., Oishi, J. S., et al. 2011, *ApJS*, 192, 9, doi: [10.1088/0067-0049/192/1/9](https://doi.org/10.1088/0067-0049/192/1/9)
- van de Voort, F., Springel, V., Mandelker, N., van den Bosch, F. C., & Pakmor, R. 2019, *MNRAS*, 482, L85, doi: [10.1093/mnrasl/sly190](https://doi.org/10.1093/mnrasl/sly190)
- van Woerden, H., Wakker, B. P., Schwarz, U. J., & de Boer, K. S., eds. 2004, *Astrophysics and Space Science Library*, Vol. 312, High Velocity Clouds
- Veilleux, S., Cecil, G., & Bland-Hawthorn, J. 2005, *ARA&A*, 43, 769, doi: [10.1146/annurev.astro.43.072103.150610](https://doi.org/10.1146/annurev.astro.43.072103.150610)
- Voit, G. M., Donahue, M., Zahedy, F., et al. 2019, *ApJL*, 879, L1, doi: [10.3847/2041-8213/ab2766](https://doi.org/10.3847/2041-8213/ab2766)
- Wakker, B. P. 1991, *A&A*, 250, 499
- . 2001, *ApJS*, 136, 463, doi: [10.1086/321783](https://doi.org/10.1086/321783)
- Wakker, B. P. 2004, in *Astrophysics and Space Science Library*, Vol. 312, High Velocity Clouds, ed. H. van Woerden, B. P. Wakker, U. J. Schwarz, & K. S. de Boer, 25
- Wakker, B. P., Savage, B. D., Fox, A. J., Benjamin, R. A., & Shapiro, P. R. 2012, *ApJ*, 749, 157, doi: [10.1088/0004-637X/749/2/157](https://doi.org/10.1088/0004-637X/749/2/157)
- Wakker, B. P., & van Woerden, H. 1997, *ARA&A*, 35, 217, doi: [10.1146/annurev.astro.35.1.217](https://doi.org/10.1146/annurev.astro.35.1.217)
- Wakker, B. P., York, D. G., Wilhelm, R., et al. 2008, *ApJ*, 672, 298, doi: [10.1086/523845](https://doi.org/10.1086/523845)
- Wakker, B. P., York, D. G., Howk, J. C., et al. 2007, *ApJL*, 670, L113, doi: [10.1086/524222](https://doi.org/10.1086/524222)
- Watkins, L. L., Evans, N. W., & An, J. H. 2010, *MNRAS*, 406, 264, doi: [10.1111/j.1365-2966.2010.16708.x](https://doi.org/10.1111/j.1365-2966.2010.16708.x)
- Watkins, L. L., van der Marel, R. P., Sohn, S. T., & Evans, N. W. 2019, *ApJ*, 873, 118, doi: [10.3847/1538-4357/ab089f](https://doi.org/10.3847/1538-4357/ab089f)
- Werk, J. K., Prochaska, J. X., Thom, C., et al. 2013, *ApJS*, 204, 17, doi: [10.1088/0067-0049/204/2/17](https://doi.org/10.1088/0067-0049/204/2/17)
- Werk, J. K., Prochaska, J. X., Tumlinson, J., et al. 2014, *ApJ*, 792, 8, doi: [10.1088/0004-637X/792/1/8](https://doi.org/10.1088/0004-637X/792/1/8)
- Werk, J. K., Rubin, K. H. R., Bish, H. V., et al. 2019, arXiv e-prints, arXiv:1904.11014, <https://arxiv.org/abs/1904.11014>
- Zahedy, F. S., Chen, H.-W., Johnson, S. D., et al. 2019, *MNRAS*, 484, 2257, doi: [10.1093/mnras/sty3482](https://doi.org/10.1093/mnras/sty3482)
- Zheng, Y., Peek, J. E. G., Putman, M. E., & Werk, J. K. 2019a, *ApJ*, 871, 35, doi: [10.3847/1538-4357/aaf6eb](https://doi.org/10.3847/1538-4357/aaf6eb)
- Zheng, Y., Peek, J. E. G., Werk, J. K., & Putman, M. E. 2017, *ApJ*, 834, 179, doi: [10.3847/1538-4357/834/2/179](https://doi.org/10.3847/1538-4357/834/2/179)
- Zheng, Y., Putman, M. E., Peek, J. E. G., & Joung, M. R. 2015, *ApJ*, 807, 103, doi: [10.1088/0004-637X/807/1/103](https://doi.org/10.1088/0004-637X/807/1/103)
- Zheng, Y., Putman, M. E., Emerick, A., et al. 2019b, *MNRAS*, 490, 467, doi: [10.1093/mnras/stz2563](https://doi.org/10.1093/mnras/stz2563)